

Technical Report

TR-15-08

Januari 2016



Long-term performance of the bentonite barrier in the SFR silo

Peter Cronstrand

SVENSK KÄRNBRÄNSLEHANTERING AB

SWEDISH NUCLEAR FUEL
AND WASTE MANAGEMENT CO

Box 250, SE-101 24 Stockholm
Phone +46 8 459 84 00
skb.se

SVENSK KÄRNBRÄNSLEHANTERING

ISSN 1404-0344

SKB TR-15-08

ID 1486771

January 2016

Long-term performance of the bentonite barrier in the SFR silo

Peter Cronstrand, Westinghouse Electric Sweden AB

This report concerns a study which was conducted for Svensk Kärnbränslehantering AB (SKB). The conclusions and viewpoints presented in the report are those of the author. SKB may draw modified conclusions, based on additional literature sources and/or expert opinions.

A pdf version of this document can be downloaded from www.skb.se.

© 2015 Svensk Kärnbränslehantering AB

Summary

The long-term function of the bentonite layer surrounding the silo in SFR has been assessed through reactive-transport modelling. As long as the concrete wall is intact, the degradation proceeds at a much lower rate and the degradation depth is predicted to be approximately 20 cm and localized to the interface between the concrete and the bentonite. In principle the alteration depth can be assumed to be in scale with the mean square displacement, *i.e.* proportional to the square root of time and diffusivity. Fractured concrete resulting in extensive exposure to fresh cement pore water has on the other hand a significant alteration effect on the montmorillonite. However the amount of fresh cement pore water is limited and cement pore water in equilibrium with portlandite and later CSH, has a minor effect on the dissolution rate of montmorillonite. The selection of models employed exhibits low sensitivity, except for the choice of database. The composition of the water released from the repository is for the most part constant throughout the period of time considered and the predicted variations are probably insignificant compared with natural variations due to more global geological processes.

Sammanfattning

De långsiktiga egenskaperna hos det bentonitskikt som omger silon i SFR har bedömts genom reaktiv transportmodellering. Så länge betongväggen är intakt, går nedbrytningsprocesserna i bentoniten mycket långsamt och endast de 20 cm av bentoniten som ligger närmast betongen påverkas. I princip kan förändringsdjupet beskrivas som proportionellt mot medelkvadratförskjutningen (\sqrt{Dt}). Sprucken betong leder till en ökad exponering av bentoniten för porvatten från färsk betong. Detta färska betongporvatten kan orsaka stora mineralförändringar i bentoniten. Dock är mängden sådant porvatten mycket begränsad. Så snart den initiala porvattenvolymen bytts ut mot ett portlanditjämviktat (och senare CSH-jämviktat) porvatten minskar förmågan att ändra på mineralsammansättningen i bentoniten. De modeller som använts har visats ge mycket liknande resultat, med undantag av valet av termodynamisk databas. Vattensammansättningen i förvaret har antagits vara konstant under den tidsperiod som omfattas av denna undersökning. De förmodade små variationer som kan uppstå i vattensammansättningen på avfallssidan av barriären kan antas vara mindre betydande för resultatet av denna undersökning än andra geologiska processer av mer global natur.

Contents

1	Introduction	7
1.1	Purpose	7
1.2	Background	7
2	Method of approach	9
2.1	Degradation of cement	9
2.2	Composition of bentonite	10
2.3	Conceptual degradation of bentonite	12
2.4	Long term chemical stability of bentonite in a repository environment	14
2.4.1	Mass balance	14
2.4.2	Mass transport	16
2.4.3	Reaction kinetics	19
3	Input data	21
3.1	Chemical characterization of adjacent barriers	21
3.2	Mineralogy and pore water composition	22
3.2.1	Primary minerals	22
3.2.2	Secondary minerals	23
3.2.3	Kinetics	25
3.3	Transport properties	25
3.3.1	Diffusivities	25
3.3.2	Ion exchange and surface complexation	25
3.4	Infiltrating water	26
3.5	Computational details	26
3.5.1	Silo model	26
3.5.2	Database and program	27
3.5.3	Model cases	27
4	Results	29
4.1	Integrity of the bentonite layer	29
4.2	The composition of the water released from the repository	34
5	Comments and conclusions	35
5.1	Uncertainties	35
5.1.1	Uncertainties in mechanistic understanding	35
5.1.2	Model simplifications	36
5.1.3	Input data and data uncertainty	36
5.1.4	Overall uncertainties	36
	References	37
Appendix A	Summary of input data for primary and secondary mineral phases	41
Appendix B	Evolution of the bentonite barrier	43

1 Introduction

1.1 Purpose

The purpose of the report is to assess the long-term composition of the bentonite layer surrounding the Silo in terms of mineralogy, pore water composition and the composition of the water outside the silo from a reactive-transport modelling approach. The models will comprise:

- Batch calculations of mineralogical changes in montmorillonite associated with pore water exchanges with pore water released from concrete.
- Reactive-transport calculations of various one-dimensional models for the Silo, including parameter variation. The models will partly be based on the work accomplished in Cronstrand (2007).

1.2 Background

The primary barrier function of the bentonite layer surrounding the Silo at SFR is to ensure a low hydraulic conductivity. The montmorillonite in the bentonite binds water and increases in volume. This process would cause the bentonite to swell, but since the clay is confined to the space between the rock and the concrete barrier the water uptake will instead decrease the porosity – and thus increase the density – of the clay layer. The decrease in porosity will make the clay layer impermeable to water transport, which in hydraulic transport modelling manifests as a low hydraulic conductivity in the bentonite. The confined swelling also gives rise to a swelling pressure on the confining walls. The low hydraulic conductivity is thus closely related to a high swelling pressure. The long-term function of the repository is thereby strongly dependent on the swelling pressure, which in turn is a function of the content of montmorillonite in the clay (Sato 2008). The dependence is thoroughly summarized for a wide selection of bentonite clays in Karnland et al. (2006). The swelling pressure and the hydraulic conductivity as a function of density for a reference sample of MX-80 are shown in Figure 1-1, from Karnland et al. (2006).

However, during the life-time of the repository the montmorillonite will be affected by the high-alkaline water released from the adjacent concrete, but also from the infiltrating groundwater, which composition will gradually change due to land uplift. Under less favourable conditions montmorillonite can be converted to minerals with similar structure, but with significantly decreased swelling capacity. The conversion process is not entirely revealed, but is believed to be initiated by dissolution of silica followed by a charge re-distribution, which mechanisms permanently destabilize the clay-water structure (Pusch 1993, Pusch et al. 2009). Less charge re-distribution is required for potassium than for sodium as the interlayer cation. Whereas potassium is associated with conversion to illite, sodium is associated with brammallite/rectorite (Karnland and Birgersson 2006). Conversion to chlorite has also been observed but is presumed to be a slower process with less detrimental consequences for swelling pressures (Karnland and Birgersson 2006). If iron occurs in the montmorillonite structure, there will also be additional sensitivity towards redox-changes. Although the mechanism for montmorillonite dissolution is not completely understood, the conversion to illite has been pointed out as the most important detrimental process in a repository environment (Karnland and Birgersson 2006). Several kinetic relations have historically been proposed (Elliot et al. 1996), but since the dissolution of silica in general is dependent on pH, none of the relations has been applicable to the conditions created by cement pore water. More recent studies with special emphasis on the pH dependency of the dissolution of montmorillonite (Rozalén et al. 2008, 2009, Sato et al. 2003) proposes kinetic relations valid over a full pH range 1–13.5. By combining the kinetic relations with thermodynamic databases it is possible to describe the aging of the bentonite layer surrounding the Silo in terms of mineralogical alteration through reactive-transport modelling.

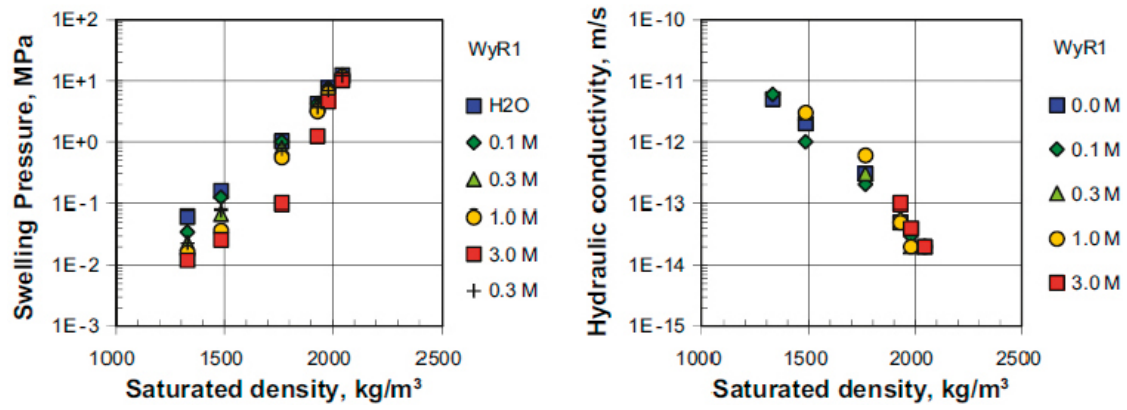


Figure 1-1. Swelling pressure and hydraulic conductivity as a function of density for MX-80 for a selection of NaCl solutions, from Karnland (2010).

2 Method of approach

2.1 Degradation of cement

Cement-based materials are characterized by an equilibrium between different mineral phases, primarily crystalline portlandite ($\text{Ca}(\text{OH})_2$) and amorphous to crypto-crystalline Calcium Silica Hydrate (CSH). Portlandite is a well-defined mineral phase, which will stabilize the pH at 12.4. CSH on the other hand lacks an unequivocal stoichiometry and the incongruent dissolution is characterized by a gradual decrease in calcium/silica ratio accompanied by a pH decrease from 12.4 down to 11.

Other mineral phases, such as the water-rich minerals AFm (calcium alumina/ferric oxide monosulphate/carbonate hydrate), as monosulphate $[(\text{CaO})_3(\text{Al,Fe})_2\text{O}_3)(\text{CaSO}_4)\cdot(\text{H}_2\text{O})_{12}]$ and monocarbonate $[(\text{CaO})_3(\text{Al,Fe})_2\text{O}_3)(\text{CaCO}_3)\cdot(\text{H}_2\text{O})_{12}]$, and Aft (calcium alumina/ferric oxide tri-sulphate (/carbonate) hydrate), as ettringite $[(\text{CaO})_3(\text{Al,Fe})_2\text{O}_3)(\text{CaSO}_4)_3\cdot(\text{H}_2\text{O})_{32}]$ are essential in the formation of cement, but contribute with only a fraction of the bulk material and have less influence on the composition of the pore water released from the concrete matrix.

The typical long-term degrading mechanism causing aging of cement is the inward and outward transport of ions, which disrupts the prevailing equilibriums and enables dissolution and precipitation of various mineral phases. The leaching of ions and the accompanying mineral changes can be monitored by successive pH-drops. While alkali hydroxides in the initial pore water maintain the high pH at 13.5, their leaching will lower the pH to 12.4, where the pH mainly is controlled by portlandite. The subsequent pH drop between 12.5 and 10.5 is characterized by the incongruent dissolution of CSH. Figure 2-1 shows the typical degradation scheme as predicted by the Thermoddem database (Blanc et al. 2007) for concrete when exposed to leaching by demineralized water. For each leaching step a fraction of the water is replaced with fresh water, which displaces the equilibrium and degrades the material by changing the mineral composition. The time scale and predicted mineral distribution is highly sensitive to the exchange rate and the composition of the infiltrating water, especially at late stage degradation where non-cementitious mineral phases dominate the precipitation. Thus, the pore water released from cement will vary in composition as well as pH, from the initial flush of hyperalkaline water (pH 13.5) dominated by NaOH, KOH, through the less alkaline waters (pH 12.5) controlled by the dissolution of $\text{Ca}(\text{OH})_2$, to the late stage waters (pH 12.5–11) with increasing levels of Si in equilibrium with decalcified CSH. Although the actual release of pore water from the cement to a large extent will be controlled by diffusion processes it still possible from the degradation scheme to distinguish between three different types of water, see Table 2-1.

Typical cement pore water for fresh cement and cement with a remaining fraction portlandite controlling the pH are in agreement with cement pore water determined in experimental investigations by Andersson et al. (1989) and Berner (1992) as well as the water employed in modelling studies as Savage et al. (2011) and Fernández et al. (2010).

Table 2-1. Typical composition of cement pore water for fresh cement, cement with remaining portlandite and cement with decalcified CSH.

	Fresh cement (M)	Portlandite (M)	Decalcified CSH (M)
pH	13.5	12.4	11
Al	5.64×10^{-4}	6.55×10^{-5}	4.29×10^{-7}
Ca	7.93×10^{-4}	1.72×10^{-2}	1.15×10^{-3}
Cl	4.91×10^{-2}		
Fe	2.30×10^{-8}		
K	4.06×10^{-1}		
Mg	3.01×10^{-10}	2.79×10^{-9}	8.58×10^{-7}
Na	1.47×10^{-1}		
S	2.73×10^{-3}	8.84×10^{-6}	
Si	9.63×10^{-5}	2.99×10^{-6}	1.42×10^{-3}

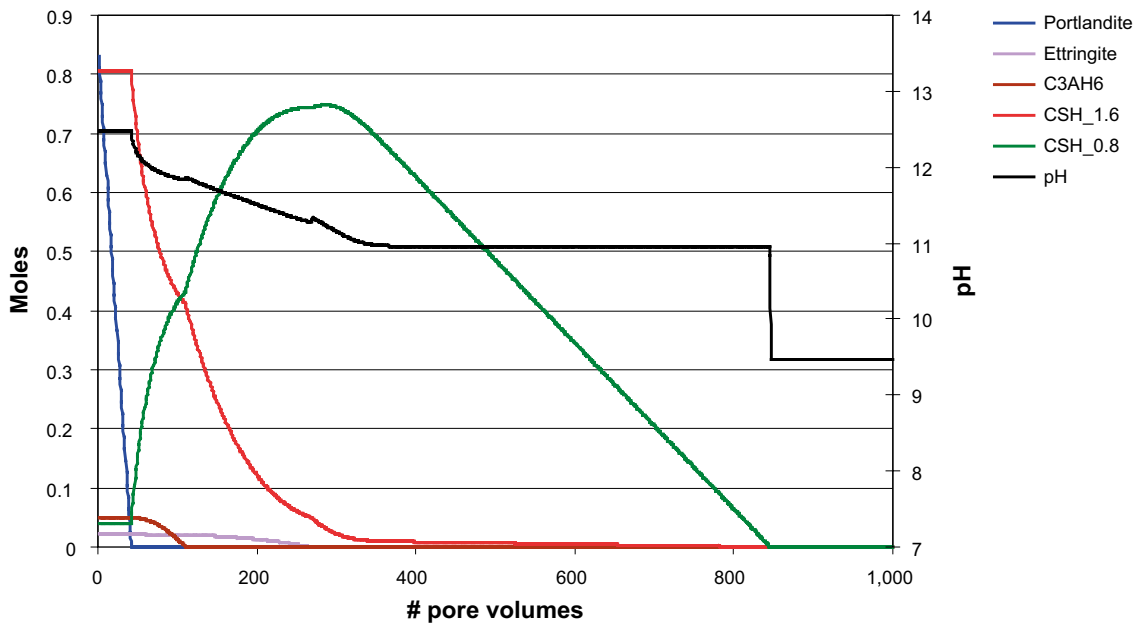
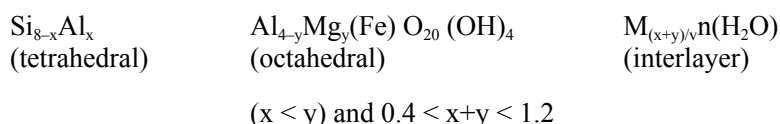


Figure 2-1. Typical degradation scheme of concrete when exposed to demineralised water as predicted by *phreeqc* in combination with *Thermodynam* database. *CSH_1.6* and *CSH_0.8* form the end members in a solid solution representing the CSG gel.

It is emphasized that there are significant differences in total available amounts of the cement pore waters characterized in Table 2-1. Whilst the initial fresh cement pore water is not stabilized by any mineral phases, the long-term waters will be in equilibrium with portlandite and later CSH. Thus, the fresh cement pore water will be replaced in one single pore water exchange, the portlandite-water approximately 40 pore water exchanges and CSH several hundreds of pore water exchanges. The general guidelines for long-term impact on the bentonite barrier from concrete pore water can mainly be derived from the two latter types of water.

2.2 Composition of bentonite

Bentonite is a generic term for smectite clays with a varying but always high fraction of montmorillonite. The structure of montmorillonite is generally perceived as an alumina octahedral sheet sandwiched between two tetrahedral silica sheets. Each tetra-octa-tetra (T-O-T) layer is approximately 1 nm. Isomorphous substitution of the cations by cations of lower valency, Al^{3+} replacing Si^{4+} (number of substitutions denoted x) in the tetrahedral layer and Mg^{2+} replacing Al^{3+} (number of substitutions denoted y) in the octahedral layer, is manifested as a permanent negative charge of the clay platelet.



Employing the unit cell of pyrophyllite proposed by Skipper et al. (1995) and the corresponding isomorphous substitutions (Chávez-Páez et al. 2001) the structure of pyrophyllite and Wyoming montmorillonite can be visualized as Figure 2-2.

The stoichiometric representation of a unit cell of montmorillonite frequently employed in thermodynamic databases is $\text{Na}_{.33}\text{Mg}_{.33}\text{Al}_{1.67}\text{Si}_4\text{O}_{10}(\text{OH})_2$. The specific surface area is often assumed to be on the order of $800 \text{ m}^2/\text{g}$, while the BET analysis on dry material often is determined to be much lower, $30\text{--}80 \text{ m}^2/\text{g}$, (Karland 2010) since the interlayer in dry material is inaccessible to nitrogen gas. The total permanent negative charge is characterized by the cation exchange capacity (CEC), which for montmorillonite is on the order of $0.8 \text{ eq}/\text{kg}$.

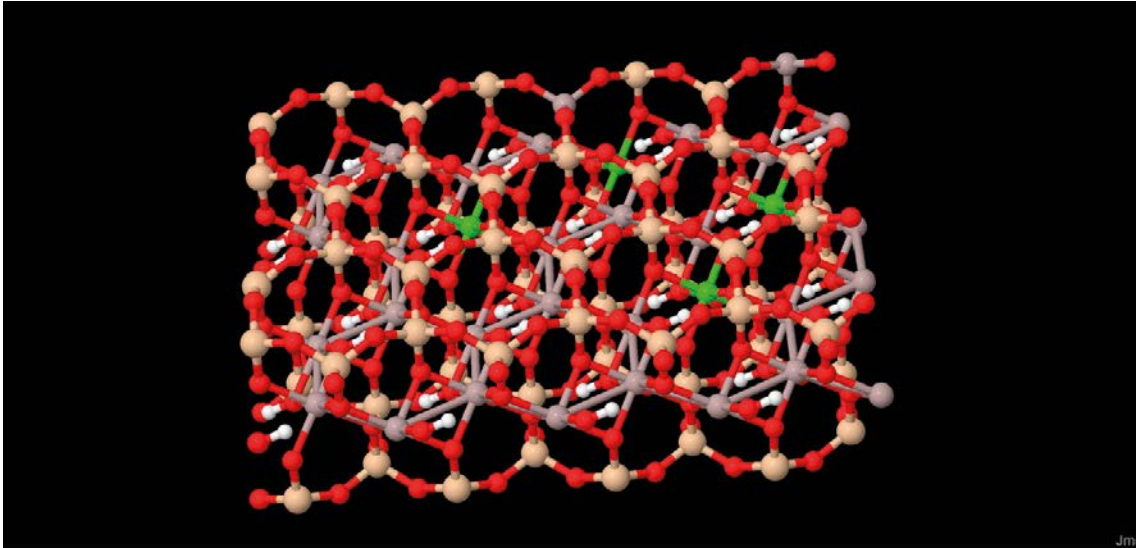


Figure 2-2. Model of one sheet montmorillonite, the substitutions of Al by Mg denoted by the colour green.

An excess of charge-compensating cations, typically Na, Ca and K, maintain charge neutrality and constitute an electrical double layer between the clay platelets. The swelling capacity of the clay is to a large extent determined by the valence and type of cation in between the clay platelets. The subsequent swelling results in a less well ordered structure and are denoted osmotic swelling.

Along with the permanent charge deficits in the octa- and tetrahedral structure, there is also a second type of reactive site associated with amphoteric surface hydroxyl groups localized along the edges of the clay particle/crystals. The sites represented by $=\text{SOH}$, can protonate ($=\text{SOH}_2^+$) and deprotonate ($=\text{SO}^-$) and adapt to the pH of the solution. The number of sites are in general assumed to be $0.04\text{--}0.08 \text{ mol kg}^{-1}$, *i.e.* 5–10% of the available exchange sites (Bradbury and Baeyens 2003).

The layered structure of montmorillonite determines the swelling pressure and the low hydraulic conductivity, but also the ion exchange properties and thereby also the transport properties of the material. Because of the net charge of the clay platelets, cations and anions will experience different surface electrical effects when diffusing through the material. The observed differences in transport times have either been interpreted as differences in geometrical factors for anions and cations (Appelo et al. 2010, Bourg et al. 2003, 2007, Melkior et al. 2004, Van Loon et al. 2007), applying Donnan equilibrium (Birgersson and Karnland 2009) or a thorough electrochemical analysis (Leroy et al. 2006).

The first approach often applies a distinction between free porosity water and water bound to the electrical double layer. Whereas anions solely diffuse through the fraction of free water, the transport of cations is envisaged to take place both in free water and through diffuse double layer. Thus, the diffusion of cations will to a larger extent occur in free water at higher ionic strengths, as the diffuse layer is compressed.

The alternative approach (Birgersson and Karnland 2009) assumes one single type of porosity, but supplements cation exchange with Donnan equilibrium in order to describe the apparent anion exclusion effects.

In spite of the differences in theoretical assumptions, both approaches enable to satisfactorily model the diffusive transport for both cations and anions.

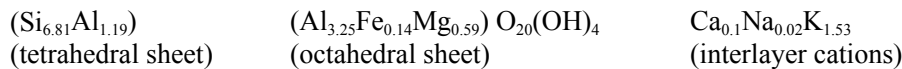
In addition to the montmorillonite, bentonite contains minor fractions of other mineral phases such as quartz, feldspar, muscovite. Table 2-2 summarizes the average mineralogy of the type of bentonite marketed as MX-80.

Table 2-2. Average mineralogy for MX-80 (Karnland et al. 2006).

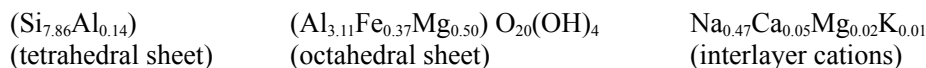
Phase	Wt. %
Montmorillonite	83.5
Illite	0.7
Anatase	0.2
Calcite	0.2
Cristobalite	0.4
Goethite	0.2
Gypsum	0.9
Hematite	0.1
Lepidocrocite	0.7
Magnetite	0.1
Microcline	0.8
Muscovite	2.8
Orthoclase	0.7
Plagioclase	2.9
Pyrite	0.6
Quartz	2.8
Tridymite	1.9

2.3 Conceptual degradation of bentonite

The first attempts to quantitatively assess the chemical stability of smectite have been evaluated from geological data (Velde and Vasseur 1992, Pytte and Reynolds 1989, Huang 1992) where the changes in illite smectite composition have been determined in illite/smectite interstratified minerals with well-known burial history. Whereas the structure of the illite can be written in the form



the structure of the montmorillonite in the MX-80 SR-CAN reference bentonite can be written:



The differences between illite montmorillonite are characterized by a larger extent of Si to Al substitution in the tetrahedral layer. The significantly higher fraction of potassium interlayer cations has been interpreted as if potassium has a key-role in the degradation during neutral conditions, which is manifested in some of the rate equations suggested to describe the degradation rate. The initial step in the degradation sequence has often been described as cation exchange followed by beidellitization or illitization. In the beidellitization process aluminium replaces silica in the tetrahedral position, while magnesium occupies the positions formerly occupied by aluminium. The proposed rate equations are all of the type

$$\frac{\partial S}{\partial t} = -\kappa S^\alpha ([K^+])^\beta \quad (2-1)$$

where the actual rate constant is assumed to be of Arrhenius type, *i.e.*

$$\kappa = -Ae^{(-E_a/RT)} \quad (2-2)$$

Unlike Pytte and Huang, Velde assumes a two-step model, where the smectite first is converted to random ordered illite/smectite and then to ordered illite/smectite. The kinetic expressions and the parameter values are summarized in Table 2-3. In spite of the individual differences, all expressions can reproduce the transformation of smectite to illite in geological settings (Elliot et al. 1996), however since none of the expression includes an explicit dependence on pH, they are less applicable to the high-alkaline conditions expected near a cement based repository.

Table 2-3. Early kinetic expressions for smectite-illite conversion.

Model	Kinetic expression	Parameter values
Pytte and Reynolds 1982	$\frac{\partial S}{\partial t} = -\kappa S^\alpha \left(\frac{[K^+]}{[Na^+]} \right)^\beta$	$\alpha=4$ $\beta=1$ $E_a = 125.52$ (kJ/mole) $A = 9.00 \times 10^4$ s
Huang 1992	$\frac{\partial S}{\partial t} = -\kappa S^\alpha [K^+]^\beta$	$\alpha=2$ $\beta=1$ $E_a = 117.15$ (kJ/mole) $A = 8.08 \times 10^4$ s
Velde and Vasseur 1992	$\frac{\partial S}{\partial t} = -\kappa_1 S$ $\frac{\partial M}{\partial t} = \kappa_1 S - \kappa_2 M$	$\alpha=1$ $E_a^1 = 37.24$ (kJ/mole) $E_a^2 = 67.78$ (kJ/mole) $A_1 = 8.08 \times 10^4$ s $A_2 = 6.9 \times 10^{-5}, 4.25 \times 10^{-11}$

Although the dissolution mechanism in high-alkaline conditions is not completely understood (Takahashi et al. 2007, Rozalén et al. 2009), the dissolution process is assumed to be significantly accelerated in accordance with the general enhanced solubility of silica species (see Figure 2-3). In the later stages of dissolution, zeolites and crystallized Ca phases as CSH, tobermorite and calcite may form.

Other studies (Huertas et al. 2001, Fujiwara et al. 2003, Sato et al. 2003, Rozalén et al. 2008) with focus on high alkaline conditions have suggested higher dissolution rates, but have not explicitly made any distinction between the effects associated with potassium vs. sodium. It has been pointed out that the development of simplified models is limited by the complexity of the montmorillonite edge structure.

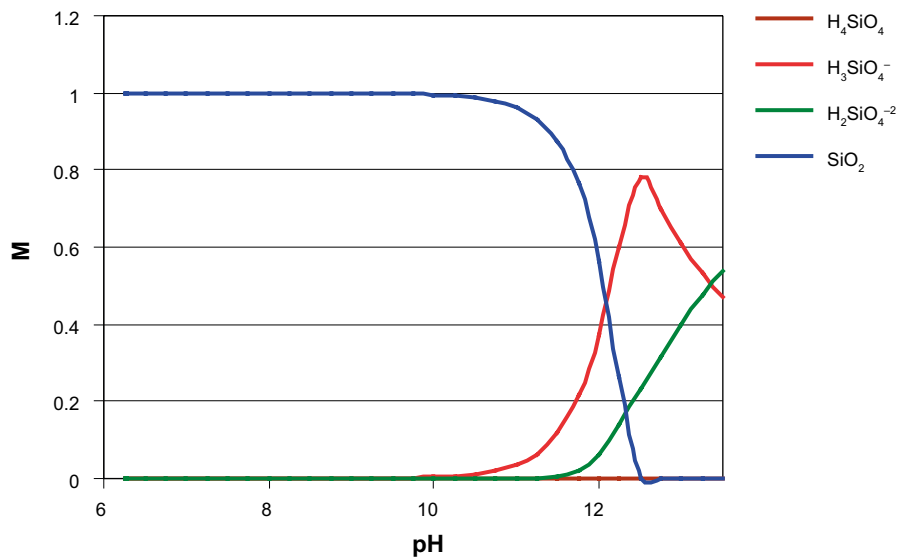


Figure 2-3. Stability of silica as function of pH as predicted by PHREEQC and phreeqc.dat database.

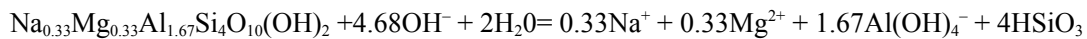
2.4 Long term chemical stability of bentonite in a repository environment

Although montmorillonite *per se* is thermodynamically unstable in high-alkaline conditions, the long-term chemical stability of bentonite is controlled through various constraints, *i.e.*:

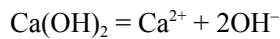
- Constraint by mass balance
- Constraint by mass transport
- Constraint by reaction kinetics

2.4.1 Mass balance

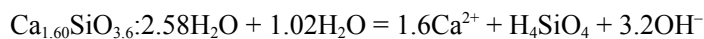
The typical dissolution reaction proposed by thermodynamic databases (here Thermoddem) is:



Within this representation, 1 mole montmorillonite consumes 4.68 moles OH^- during dissolution reaction. With montmorillonite having a molar mass of 367.017 (≈ 400) g/mol, and a dry density of 1.5 g/cm³, 1 l of buffer with a porosity of 0.6 (400 cm³ solid) corresponds to 1.5 moles of montmorillonite. Thus 1 l of buffer consumes approximately 7 moles of OH^- during dissolution. Concrete on the other hand releases OH^- through dissolution of portlandite

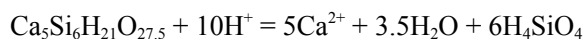


and through dissolution of CSH

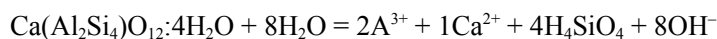


Assuming 1 l of pure cement corresponds to 3.5 moles of CSH and 3.4 moles portlandite, the total amount of OH^- -released from 1 l cement can be estimated to 18 moles. Thus, 1 m³ pure cement can at maximum affect approximately 2.5 m³ bentonite. For concrete containing a significant amount of ballast, the ratio between cement and bentonite is substantially lower and the corresponding volume ratios are on the order of 1:1 or 1:0.5 cement/bentonite. However, these estimates are based on total mass balances and do not reflect the dependence on concentration/pH. If a certain threshold is required for montmorillonite dissolution, such that only pore water from fresh cement can result in montmorillonite dissolution, the corresponding relations between volumes affected bentonite and affecting concrete will change dramatically. If 1 l of bentonite buffer requires 7 moles of OH^- , approximately 23 l of pore water with pH 13.5 is needed to dissolve 1 l bentonite. For concrete with a porosity of 0.15, 23 l of pore water corresponds to 150 l concrete. Thus, under the assumption that only extremely alkaline water from fresh cement will affect the bentonite, mass balance suggests that 1 volume unit of bentonite requires at least 100 volume units of concrete.

The rough estimate excludes any constraints due to transport or precipitation of a sequence of secondary minerals. For instance, the precipitation of tobermorite



will consume OH^- , whereas at lower pH conditions, the precipitation of for instance laumontite



will generate OH^- .

Hence, at higher pH, OH^- can temporarily be stored in precipitated secondary minerals and gradually return to the solution when dissolving in a non-linear fashion. The mechanism can potentially retard pH decrease and the dissolution of montmorillonite, but most likely introduce a non-linear dissolution pattern.

The mineral alteration following the high-alkaline plume will be strongly dependent on the composition of the water. The mineral alteration as predicted by Thermoddem database for a sequence of complete pore water exchanges with KOH, NaOH and $\text{Ca}(\text{OH})_2$ is summarized in Figures 2-4 to 2-6. Although the dissolution rates are comparable, pore water exchange with KOH will lead to precipitation of phillipsite and illite, whereas pore water exchange with NaOH will initially result in phillipsite

followed by analcime with minor fractions of saponite. In scenarios where pore water is exchanged with $\text{Ca}(\text{OH})_2$, the dissolution of montmorillonite is initially followed by precipitation of heulandite and some phillipsite, but at later stages precipitation is dominated by tobermorite with some fractions of gibbsite.

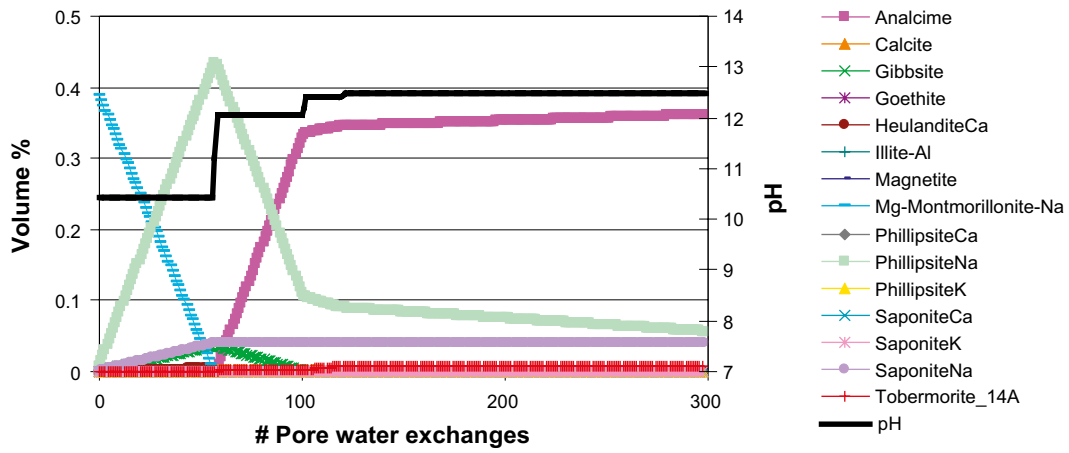


Fig 2-4. Thermodynamic prediction of degradation of bentonite as a function of pore water exchange with 0.04 M NaOH.

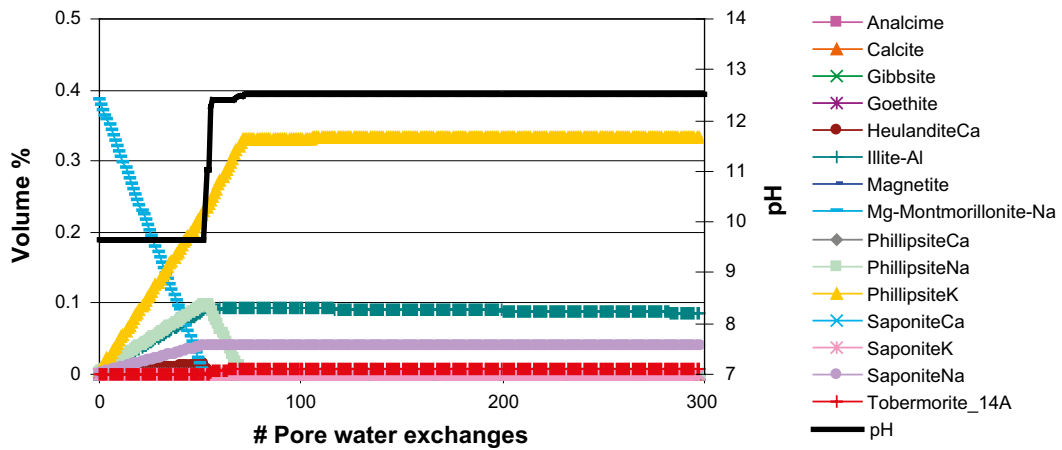


Fig 2-5. Thermodynamic prediction of degradation of bentonite as a function of function of pore water exchange with 0.04 M KOH.

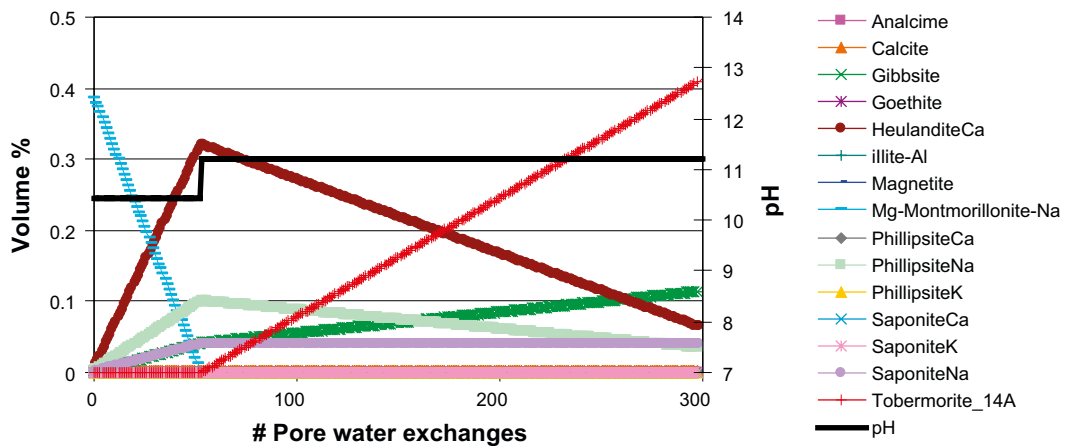


Fig 2-6. Thermodynamic prediction of degradation of bentonite as a function of pore water exchange with 0.02 M $\text{Ca}(\text{OH})_2$.

Because the initial high alkaline plume associated with fresh cement originates purely from the cement pore water and is not stabilized through any mineral phases, the total amounts of NaOH and KOH entering the bentonite will be much lower than the subsequent plume of Ca(OH)₂. Thus, Figures 2-4 to 2-6, indicate that in a full scale scenario one can initially expect the dissolution of montmorillonite to be followed by precipitation of phillipsite together with some fractions of saponite and heulandite and in the long term mainly tobermorite.

The predicted dissolution of montmorillonite and precipitation of secondary phases is sensitive to the choice of database. Figure 2-7 and 2-8 show the dissolution rate of montmorillonite and the corresponding pH response when exposed to a number of complete pore water exchanges with fresh cement pore water and cement pore water in equilibrium with portlandite as predicted by the thermodynamic databases Thermoddem, PCHatches and LLNL. According to the LLNL database, montmorillonite will be completely dissolved after 2 pore water exchanges, whereas according to PCHatches the montmorillonite can withstand 6 pore water exchanges of high alkaline water from fresh cement. For cement pore water in equilibrium with portlandite at least a factor of 10 more pore water exchanges are required for dissolving montmorillonite. According to Thermoddem and PCHatches the required numbers of pore water exchanges is on the order of 60, whilst according to LLNL at least 300 are needed.

The deviations between different databases point out one major source of uncertainty. Nevertheless, all databases agree on the scale of dissolution and that the montmorillonite can withstand several complete pore water exchanges. The robustness of the bentonite barrier will be enhanced much further when including kinetic constraints and the presumed slow transport of ions.

2.4.2 Mass transport

The diffusive transport of high-alkaline water from the cement to the bentonite layer represents a major constraint for the overall degradation process. The effective diffusion coefficients, D_e , are a function of the specific ions free diffusivity in water, D_0 , the porosity, ϵ , the geometrical factor, accounting for the tortuosity, τ , and constrictivity, δ_d , of the path through the clay and the concrete,

$$D_e = \epsilon D_0 \frac{\delta_d}{\tau^2} \quad (2-3)$$

The apparent diffusivity can be evaluated from the accessible porosity, the distribution coefficient accounting for sorption processes, K_d , and the density, ρ .

$$D_a = \frac{D_e}{\epsilon + K_d \rho} \quad (2-4)$$

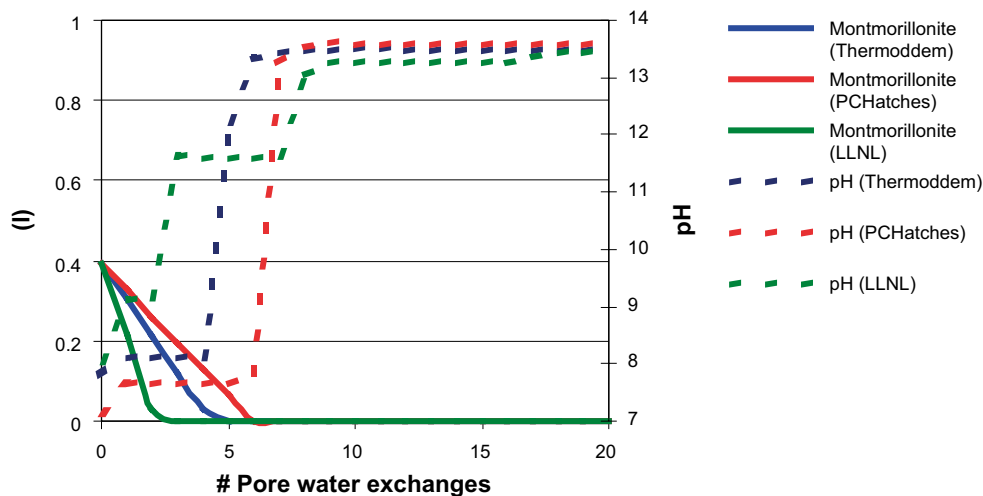


Fig 2-7. The dissolution of montmorillonite as a function of number of pore water exchanges of water from fresh cement as predicted by a selection of databases.

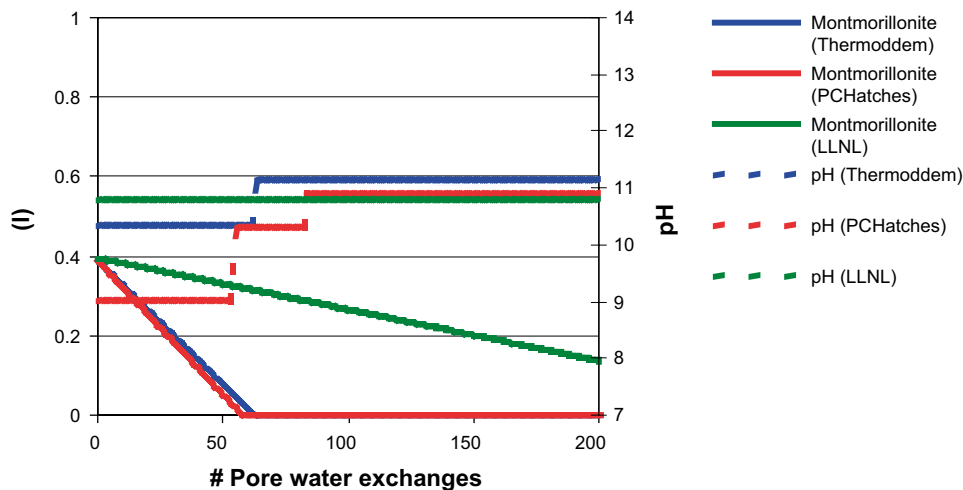


Fig 2-8. The dissolution of montmorillonite as a function of number of pore water exchanges of cement pore water equilibrated with portlandite as predicted by a selection of databases.

The concept of accessible porosity has been the most controversial component in the evaluation of the apparent porosity. One approach distinguishes between different types of pore water; inter-layer water and inter-particle water subdivided into external free water and water associated with the diffuse double layer (Wersin 2004, Apello 2011). The concurrent view does not distinguish between inter-layer and inter-particle space and argues that the montmorillonite layer is rather flexible and since the specific area is large, 800 m²/g, the total water volume is mainly localized in the interlayer. Moreover, the physico-chemical properties in the interface between montmorillonite and accessory minerals will in principle be the same as the interface between montmorillonite layers. The Donnan equilibrium view is also supported by molecular dynamics simulations (Hedström and Karnland 2012). However, both approaches have degrees of freedom, which admit fine-tuning of parameters to achieve optimum fit to observed data. In spite of differences in theoretical foundation, the consequences for the reactive-transport calculation will subordinate to other effects within the thermodynamic description of bentonite degradation.

Cation exchange and surface complexation play an important role in regulating the uptake of radionuclides as well as the pH evolution of the barrier (Bradbury and Baeyens 2009). Figures 2-9 and 2-10 show the occupancy of cation exchange sites as a function of pore water exchanges as predicted by PHREEQC and the cation exchange model by Bradbury and (Baeyens 2003). According to the model the cation distribution will change in less than 5 complete pore water exchanges from fresh cement, which is comparable with the strictly thermodynamic stability of the montmorillonite. Although there are other cation exchange models proposed for montmorillonite, their tolerance to complete pore water exchanges is on the same scale, simply due to the fact that the total amount of exchange sites is on the order of cations available in one pore volume of fresh cement water.

The major fraction, typically 95%, of available sorption sites of montmorillonite are located in between the layers and arises from charge deficiencies due to isomorphous substitutions, primarily Al³⁺ for Si⁴⁺ within the tetrahedral layer. The second category of sorption sites are located along the edges of the clay platelets and consists of surface hydroxyl groups with protonation and deprotonation reactions as a function of pH (Bradbury and Baeyens 1997). The surface hydroxyl sites provide some buffering capacity, but the number of sites are below 0.1 mol/kg, which is far less than the number of cations in one pore volume of fresh cement water. Figure 2-11 shows the distribution between protolysis states as a function of pH as predicted by PHREEQC and the surface complexation model of Bradbury and Baeyens (1997). Again, there are alternative surface complexation models proposed for montmorillonite, but their impact on the tolerance towards pore water exchanges is subordinate to thermodynamic constraints.

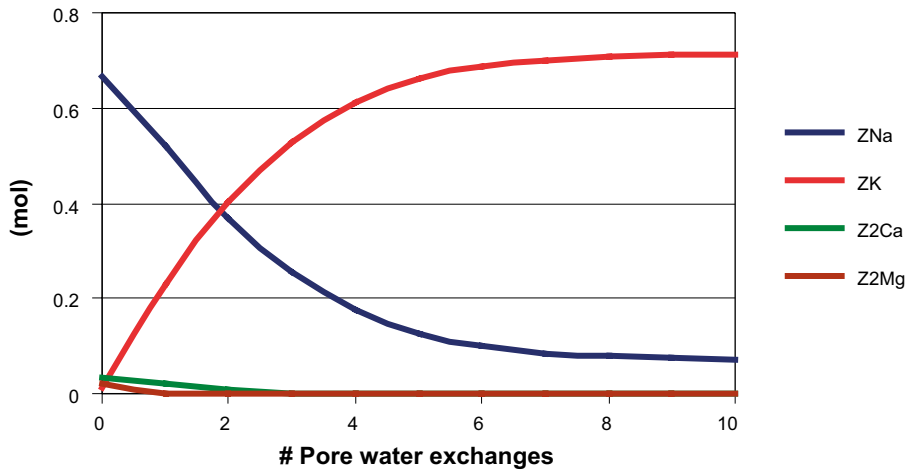


Figure 2-9. The occupancy of cation exchange sites as a function of pore water exchanges with fresh cement water (Table 2-1) as predicted by PHREEQC and the cation exchange model by Bradbury and Baeyens (2003).

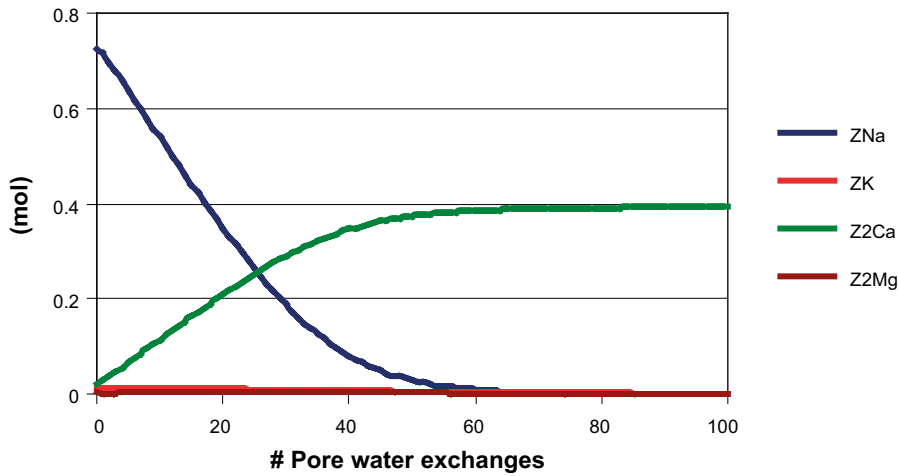


Figure 2-10. The occupancy of cation exchange sites as a function of pore water exchanges with cement water in equilibrium with portlandite (Table 2-1) as predicted by PHREEQC and the cation exchange model by Bradbury and Baeyens (2003).

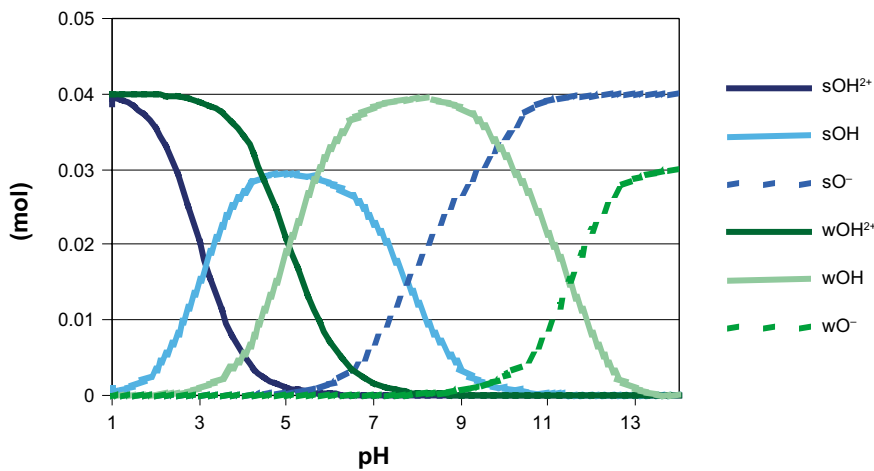


Figure 2-11. The protolysis states of strong (s) and weak (w) sites in montmorillonite as a function of pH as predicted by PHREEQC and the surface complexation model of Bradbury and Baeyens (1997).

In order to relate the constraints associated with mass balance and transport to thermodynamic constraints, it is illustrative to estimate the corresponding mean square displacement, $\overline{x^2}$ for diffusive transport in the barrier, i.e.

$$\overline{x^2} = 2Dt$$

For a diffusivity of $D=10^{-11}$ m²/s, the mean square displacement for $t=1,000$ years is approximately 0.5 m, for 10,000 years 1.8 m. Although it is not unambiguous to relate discrete processes as pore water exchanges with a continuous diffusive transport, thousands of years appear to be required in order to significantly change the pore solution on the order of a complete pore water exchange. Since the montmorillonite can withstand several complete pore water exchanges, the relevant scale for observing any substantial chemical alteration of the bulk clay barrier is at least tens of thousands of years.

2.4.3 Reaction kinetics

The dissolution of montmorillonite is further constrained by kinetics. Several models have been proposed for the kinetics of the dissolution of montmorillonite, of which only the more recent (Huertas et al. 2001, Fujiwara et al. 2003, Sato et al. 2003, Rozalén et al. 2008) include an explicit dependence on pH, see Table 2-4.

Except for the model of Sato et al. all proposed rates are within one order of magnitude, see Figure 2-12, within the desired pH range.

Table 2-4. Kinetic models for smectite to illite conversion.

Kinetic model	Rate equation	Comment
Huertas	$10^{-12.31} (a_{\text{OH}^-})^{0.34}$	
Fujiwara	$10^{-17.1} (a_{\text{H}^+})^{-0.34}$	
Sato	$10^{-13.58} (a_{\text{H}^+})^{-0.15}$	
Rozalen	$10^{-12.30} (a_{\text{H}^+})^{0.40} + 10^{-14.37} + 10^{-13.05} (a_{\text{OH}^-})^{0.27}$	Includes a neutral and acidic correction

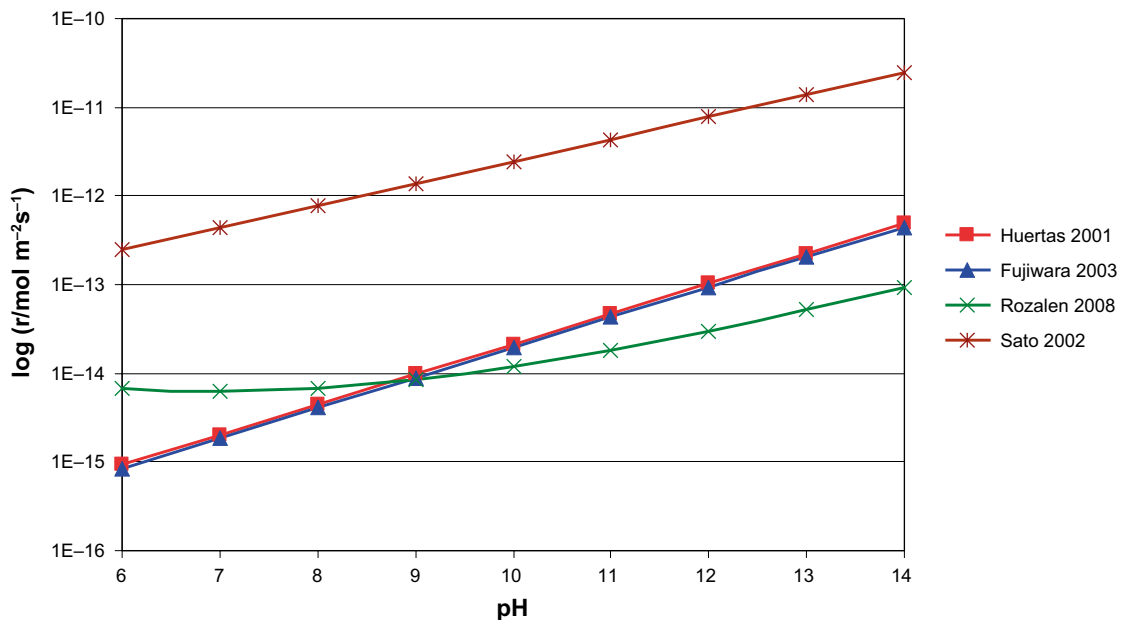


Figure 2-12. Dissolution rates for as a function of pH as suggested by Huertas et al. (2001), Fujiwara et al. (2003), Rozalén et al. (2008) and Sato et al. (2003) for $T = 25^\circ\text{C}$.

All kinetic models assume temperature dependence according to Arrhenius relation, *i.e.*

$$\kappa \propto e^{-E_a/RT} \quad (2-5)$$

The dependence on degree of saturation is in general expressed through relations derived from transition state theory, *i.e.* of the type

$$\kappa \propto \left(1 - \frac{Q}{K}\right) \quad (2-6)$$

where Q denotes ionic activity product/reaction quotient and K the equilibrium constant. Based on findings which showed a somewhat steeper dependence on the ratio Q/K , (Cama et al. 2000) suggested a modified empirical relation;

$$\kappa \propto \left(1 - a(\log(Q/K))^6\right) \quad (2-7)$$

where $a = -6 \times 10^{-10}$. A more recent attempt by Marty et al. (2011) also suggests a steeper dependence on the Gibbs energy, *i.e.* numerically the ratio Q/K and a slightly higher overall rate, but does not include any explicit pH-dependence.

$$r = 3.82 \cdot 10^{-12} \left[1 - \exp\left(-8.23 \cdot 10^{-10} \left|\frac{\Delta G_r}{RT}\right|^{5.47}\right) \right] \quad (2-8)$$

It is emphasized that the derived rates refer to far-from-equilibrium batch dissolution experiments. In compacted bentonite lower rates and a more pronounced dependence on pH have been observed. In contrast to the exponential decay obtained from widely accepted rate laws Yamaguchi et al. (2007) and Nakayama et al. (2004) suggests a linear decrease

$$W(t) = W(0) - Rt \quad (2-9)$$

where R is evaluated through

$$R = 3.5(a_{OH^-})^{1.4} \exp\left(\frac{-51,000}{RT}\right) \quad (2-10)$$

Although the rates evaluated from proposed rate equations (see Figure 2-12) may differ by almost an order of magnitude, the predicted degradation of the clay barrier will not differ particularly since the bulk of the material will remain in equilibrium for a long time. Again, relating the rate equations with the mean square displacement of diffusing ions, the bulk of the bentonite is expected to be close to equilibrium for several tens of thousands of years.

3 Input data

3.1 Chemical characterization of adjacent barriers

The chemical composition of the barriers, shotcrete, silo-wall, grout and cement-encapsulated waste are taken from Cronstrand (2007).

Table 3-1. Composition of shotcrete.

Mineral phases	(Mol)	(Volume %)
Quartz	21.07	48.3
Albite	2.140	21.5
CSH _{1,8}	0.932	10.1
Portlandite	0.898	3.0
Ettringite	0.021	1.5
Hydrogarnet	0.056	0.8
Hydrotalcite	0.007	0.2
Magnetite	0.044	0.2
Friedels salt	0.001	0.03
Porosity		15

Table 3-2. Composition of silo-wall (concrete) (w/c 0.47).

Mineral phases	(Mol)	(Volume %)
Quartz	19.636	45.0
Albite	2.167	21.7
CSH _{1,8}	1.147	12.4
Portlandite	1.111	3.7
Ettringite	0.021	1.5
Hydrogarnet	0.050	0.8
Hydrotalcite	0.008	0.2
Magnetite	0.040	0.2
Porosity		15

Table 3-3. Composition of grout (w/c 1.125).

Mineral phases	(Mol)	(Volume %)
Quartz	16.253	37.3
Albite	1.981	19.9
CSH _{1,8}	0.775	8.4
Portlandite	0.750	2.5
Ettringite	0.022	1.6
Hydrogarnet	0.046	0.7
Hydrotalcite	0.007	0.2
Magnetite	0.036	0.2
Porosity		30

Table 3-4. Composition of cement-encapsulated waste (ILW&LLW) (w/c 0.37).

Mineral phases	(Mol)	(Volume %)
CSH _{1.8}	3.522	38.0
Portlandite	3.409	11.3
Ettringite	0.079	5.8
Hydrogarnet	0.219	3.3
Hydrotalcite	0.031	0.9
Magnetite	0.169	0.8
Porosity		40

3.2 Mineralogy and pore water composition

3.2.1 Primary minerals

The chemical characterization of bentonite clay differs slightly between different modelling studies, partly due to the use of different databases. Apart from the primary constituent, montmorillonite, all authors agree on prevalence of quartz and calcite. The distribution between the residual constituents, such as albite, analcime (analcite), chalcedony, cristobalite, gypsum, halite, illite, K-feldspar differs slightly, but has less influence on the overall chemical stability.

Based on the assumption from previous studies in Table 3-5 as well as Arcos et al. (2003), Gaucher et al. (2005) and Karnland et al. (2006), the mineralogical composition of the bentonite layer in the Silo (MX-80) has been assumed to be represented by the composition summarized in Table 3-6.

According to Pusch et al. (1985) and SKB (2008) the dry density of the bentonite should be in the interval of 0.95 ton/m³ at the top and 1.12 ton/m³ at the bottom of the silo, thereby generating a swelling pressure on the order of 200–800 kPa depending on composition and ionic strength of infiltrating water. In the calculations a dry density of 1.0 ton/m³ has been assumed.

Table 3-5. Primary minerals as suggested by different authors.

Savage et al. 2002	Lehikoinen 2009	Watson et al. 2009	Fernández et al. 2010	Savage et al. 2011
Montmorillonite	Montmorillonite	Montmorillonite	Montmorillonite	Montmorillonite
Quartz	Quartz	Quartz	Quartz	Quartz
Calcite	Calcite	Calcite	Calcite	Calcite
Analcite	Albite	Albite	Albite	Gypsum
Chalcedony	Cristobalite	Cristobalite	Cristobalite	Halite
	Gypsum	Illite(Muscovite)	Illite	
	Muscovite		K-feldspar	

Table 3-6. Composition of MX-80 according to Arcos et al. (2003), Gaucher et al. (2005) and Muurinen (2009).

	(Mol)	(Volume %)
Montmorillonite	2.53	39.4
Quartz	1.29	3.0
Calcite	0.11	0.4
Phillipsite	0.006	0.1
Illite	0.005	0.1
Saponite	0.003	0.05
Magnetite	0.002	0.008
Porosity		57

Because of the large masses of montmorillonite compared to the small volumes of water, the initial pore water of compacted bentonite will be strongly buffered by the exchange capacity and the amphoteric edge sites of montmorillonite. The composition of the pore water has been assumed according to Bradbury and Baeyens (2003), see Table 3-7. Although the pore water composition shows a slight dependence on dry density, the composition derived for a dry density of 1.2 ton/m³ should be adequate for repository conditions.

Table 3-7. Pore water compositions of MX-80 for (Bradbury and Baeyens 2002). Ionic strength 0.295 and pH 8.0.

Element	(M)
C	9.72×10^{-4}
Ca	9.01×10^{-3}
Cl	2.70×10^{-3}
K	1.13×10^{-3}
Mg	6.11×10^{-3}
Na	2.20×10^{-1}
S	1.12×10^{-1}
Sr	7.90×10^{-5}

3.2.2 Secondary minerals

The key parameters regulating the mineral alteration of bentonite associated with hyperalkaline fluids are pH, Ca/Si and Si/Al ratios respectively. The secondary mineral phases expected in low-temperature cement-bentonite system have been reviewed by Savage et al. (2007) in which is concluded that more siliceous zeolite are likely to form at lower pH, whereas aluminous zeolites, illite, CASH and feldspars are predominant at higher pH. The overall mineral alteration sequence is

CSH (high Ca/Si) → CSH (low Ca/Si) → C(A)SH → Zeolites (low Si/Al) → Zeolites (high Si/Al)

The assumed selection of secondary phases in previous studies is summarized in Table 3-8. The set of mineral phases can in principle be divided into mainly the following groups;

- Calcium Silica Hydrates (CSH).
- Calcium Aluminium Silica Hydrates (CASH).
- Tectosilicates as zeolites, and members of quartz and feldspar family respectively.
- Phyllosilicates as clay minerals and miscellaneous phyllosilicates as gyrolite.
- Carbonates.
- Hydroxides.
- Sulphates/sulfides.

The chosen set of secondary mineral phases, Table 3-9, is based the predictions from chosen database, Thermodem, but also from with the requirement that the selection should include at least one member from the groups above.

Table 3-8. Groups of secondary minerals suggested by different authors.

Group	Savage et al. 2002 (EQ3/6)	Lehikoinen 2009 (Thermoddem)	Watson et al. 2009 (EQ3/6)	Fernández et al. 2010 (EQ3/6 + Thermoddem)	Savage et al. 2011 (EQ3/6)
CSH	Tobermorite	Tobermorite11A Tobermorite14A	Tobermorite	CSH Tobermorite11A	Tobermorite
CASH		Hydrogarnet			
Zeolites	Laumontite	Katoite Heulandite Phillipsite Straetlingite Analcime	Katoite Heulandite Phillipsite Analcime Clinoptilolite	Phillipsite	Katoite Phillipsite Mesolite Analcime
Feldspar	Leucite	K-feldspar	K-feldspar		Albite
Quartz		Chalcedony	Chalcedony		Chalcedony
Clay phyllosilic-ates	Muscovite Celadonite Saponite	Illite	Saponite	Saponite	Kaolinite
Other phyllosilic-ate	Gyrolite	Gyrolite		Chlorite	
Carbonate-s		Dolomite	Dolomite		Siderite
Hydroxide-s		Gibbsite Brucite	Brucite	Gibbsite Brucite Portlandite	Brucite Goethite
Sulfate/sulfides-		Monosulfate Ettringite		Ettringite	Pyrite
Other		Friedel's salt Hydrotalcite		Talc	

Table 3-9. Summary of secondary minerals.

Phase	Structure/reaction	Log k
Albite	$\text{NaAlSi}_3\text{O}_8 + 4\text{H}^+ + 4\text{H}_2\text{O} = 1\text{Al}^{+++} + 1\text{Na}^+ + 3\text{H}_4\text{SiO}_4$	2.745
Analcime	$\text{Na}_{0.99}\text{Al}_{0.99}\text{Si}_{2.01}\text{O}_6 \cdot \text{H}_2\text{O} + 3.96\text{H}^+ + 1.04\text{H}_2\text{O} = 0.99\text{Al}^{+++} + 0.99\text{Na}^+ + 2.01\text{H}_4\text{SiO}_4$	16.644
Brucite	$\text{Mg}(\text{OH})_2 + 2\text{H}^+ = 1\text{Mg}^{2+} + 2\text{H}_2\text{O}$	17.110
Chalcedony	$\text{SiO}_2 + 2\text{H}_2\text{O} = 1\text{H}_4\text{SiO}_4$	-3.454
Dolomite	$\text{CaMg}(\text{CO}_3)_2 + 2\text{H}^+ = 2\text{HCO}_3^- + 1\text{Ca}^{++} + 1\text{Mg}^{++}$	3.533
Gibbsite	$\text{Al}(\text{OH})_3 + 3\text{H}^+ = 1\text{Al}^{+++} + 3\text{H}_2\text{O}$	7.735
Goethite	$\text{FeOOH} + 2\text{H}^+ = 0.25\text{O}_2 + 1\text{Fe}^{++} + 1.5\text{H}_2\text{O}$	-8.130
Gypsum		
Gyrolite	$\text{Ca}_2\text{Si}_3\text{O}_{7.5}(\text{OH})_2 \cdot 2\text{H}_2\text{O} + 4\text{H}^+ + 1.5\text{H}_2\text{O} = 2\text{Ca}^{++} + 3\text{H}_4\text{SiO}_4$	22.340
Heulandite	$\text{Ca}_{1.07}\text{Al}_{2.14}\text{Si}_{6.86}\text{O}_{18} \cdot 6.17\text{H}_2\text{O} + 8.56\text{H}^+ + 3.27\text{H}_2\text{O} = 2.14\text{Al}^{3+} + 1.07\text{Ca}^{2+} + 6.86\text{H}_4\text{SiO}_4$	2.460
Illite	$\text{K}_{0.85}\text{Al}_{2.85}\text{Si}_{3.15}\text{O}_{10}(\text{OH})_2 + 9.4\text{H}^+ + 0.6\text{H}_2\text{O} = 2.85\text{Al}^{+++} + 0.85\text{K}^+ + 3.15\text{H}_4\text{SiO}_4$	10.437
Kaolinite	$\text{Al}_2\text{Si}_2\text{O}_5(\text{OH})_4 + 6\text{H}^+ = 2\text{Al}^{3+} + 1\text{H}_2\text{O} + 2\text{H}_4\text{SiO}_4$	6.471
Phillipsite(Ca)	$\text{Ca}_{0.5}\text{AlSi}_3\text{O}_8 \cdot 3\text{H}_2\text{O} + 4\text{H}^+ + 1\text{H}_2\text{O} = 1\text{Al}^{+++} + 0.5\text{Ca}^{++} + 3\text{H}_4\text{SiO}_4$	2.230
Phillipsite(K)	$\text{KAlSi}_3\text{O}_8 \cdot 3\text{H}_2\text{O} + 4\text{H}^+ + 1\text{H}_2\text{O} = 1\text{Al}^{+++} + 1\text{K}^+ + 3\text{H}_4\text{SiO}_4$	-0.040
Phillipsite(Na)	$\text{NaAlSi}_3\text{O}_8 \cdot 3\text{H}_2\text{O} + 4\text{H}^+ + 1\text{H}_2\text{O} = 1\text{Al}^{+++} + 1\text{Na}^+ + 3\text{H}_4\text{SiO}_4$	1.360
Portlandite	$\text{Ca}(\text{OH})_2 + 2\text{H}^+ = 1\text{Ca}^{2+} + 2\text{H}_2\text{O}$	22.810
Saponite(Ca)	$\text{Ca}_{0.17}\text{Mg}_3\text{Al}_{0.34}\text{Si}_{3.66}\text{O}_{10}(\text{OH})_2 + 7.36\text{H}^+ + 2.64\text{H}_2\text{O} = 0.34\text{Al}^{+++} + 0.17\text{Ca}^{++} + 3\text{Mg}^{++} + 3.66\text{H}_4\text{SiO}_4$	30.709
Saponite(K)	$\text{K}_{0.33}\text{Mg}_3\text{Al}_{0.33}\text{Si}_{3.67}\text{O}_{10}(\text{OH})_2 + 7.32\text{H}^+ + 2.68\text{H}_2\text{O} = 0.33\text{Al}^{+++} + 0.33\text{K}^+ + 3\text{Mg}^{++} + 3.67\text{H}_4\text{SiO}_4$	30.934
Saponite(Na)	$\text{Na}_{0.33}\text{Mg}_3\text{Al}_{0.33}\text{Si}_{3.67}\text{O}_{10}(\text{OH})_2 + 7.32\text{H}^+ + 2.68\text{H}_2\text{O} = 0.33\text{Al}^{+++} + 3\text{Mg}^{++} + 0.33\text{Na}^+ + 3.67\text{H}_4\text{SiO}_4$	27.095
Tobermorite	$\text{Ca}_5\text{Si}_6\text{H}_{21}\text{O}_{27.5} + 10\text{H}^+ = 5\text{Ca}^{2+} + 3.5\text{H}_2\text{O} + 6\text{H}_4\text{SiO}_4$	62.940

3.2.3 Kinetics

For the dissolution kinetics of montmorillonite the rate from Rozalén et al. (2008) has been assumed, partly since it offers complete terms for the pH dependence

$$rate = \left[10^{-12.30} (a_{H^+})^{0.40} + 10^{-14.37} + 10^{-13.05} (a_{OH^-})^{0.27} \right] mol \times kg^{-1} s^{-1}, \quad (3-1)$$

where the surface area has been chosen to be $800 \text{ m}^2 \text{ g}^{-1}$ (Tournassat and Appelo 2011). Alternative rate expressions show mutual deviations on the order of one magnitude, see Figure 2-9. For the dissolution of the ballast in concrete a simplified rate equation was applied, where the rate constant was selected in accordance with (Rimstidt and Barnes 1980)

$$rate = 10^{-13.7} mol \times kg^{-1} s^{-1}. \quad (3-2)$$

3.3 Transport properties

3.3.1 Diffusivities

Although the diffusivity is a specific property for each diffusing specie as well as for the corresponding bentonite composition, in particular cations compared to anions, a single value is selected primarily based on the results of by Kozaki et al. (2001). The apparent diffusivities for sodium ions have been determined for a selection of dry densities. For a dry density of typical $1,000 \text{ kg m}^{-3}$ a diffusivity of $5.0 \times 10^{-11} \text{ m}^2 \text{ s}^{-1}$ was determined (Kozaki et al. 2005). The selected diffusivity is located in the middle of the range of values compiled in Ochs et al. (2006). In order to explore the implications of a substantially higher diffusivity, a value of $5.0 \times 10^{-10} \text{ m}^2 \text{ s}^{-1}$ was also employed in an alternative scenario. Trial calculations with specific diffusivities for each specie gave rise to numerical instabilities.

3.3.2 Ion exchange and surface complexation

The ion exchange selectivity constants proposed by Bradbury and Baeyens (2003) (see Table 3-10) were employed along with total exchange capacity (CEC) of $0.734 \text{ meq kg}^{-1}$, where the specific occupancies were distributed according to Table 3-11.

The data for protonation and deprotonation at edge sites were assumed according to Table 3-12.

Table 3-10. Ion exchange constants (Bradbury and Baeyens 2003).

Ion exchange	Log K
$Zn + K^+ = ZK + Na^+$	0.6021
$2Zn + Ca^{2+} = Z_2Ca + Na^+$	0.4150
$2Zn + Mg^{2+} = Z_2Mg + Na^+$	0.3424

Table 3-11. Cation occupancies (Bradbury and Baeyens 2003).

Cation	Cation occupancies (mol kg^{-1})
Na	0.668
K	0.013
Mg	0.020
Ca	0.033

Table 3-12. Site type, capacity, reaction and constants for montmorillonite (Bradbury and Baeyens 1997, 2003).

Site type	Site capacity (mol kg ⁻¹)	Surface complexation reaction	Log K
SwOH	0.04	SwOH + H ⁺ = SwOH ₂ ⁺	4.5
		SwOH = SwO ⁻ + H ⁺	-7.9
SsOH	0.04	SsOH + H ⁺ = SsOH ₂ ⁺	6.0
		SsOH = SsO ⁻ + H ⁺	-10.5

3.4 Infiltrating water

The composition of the infiltrating water is for the base case assumed to be the SFR water in Table 3-13, which is the same as employed in Cronstrand (2007).

Table 3-13. Composition of infiltrating water (SFR water).

	SFR water (M)
C	6.70 × 10 ⁻³
Ca	2.26 × 10 ⁻³
Cl	8.22 × 10 ⁻²
K	1.62 × 10 ⁻³
Mg	8.27 × 10 ⁻³
Na	9.32 × 10 ⁻²
S	1.35 × 10 ⁻²

3.5 Computational details

3.5.1 Silo model

The models for the Silo is constructed from a 1D system of adjacent cell in contact with boundary cells containing the infiltrating water, see Table 3-14. Whereas the outer boundary condition, as encoded by cell 0, is considered as fixed, the inner boundary condition is considered as closed and the last cell is only affected by its neighbour to the left.

Table 3-14. The system of cells constituting the model of the Silo.

Cell no	Length (m)	Material	Initial porosity
0-1		Ambient water	
2	0.1	Shotcrete	0.15
3-27	0.05	Bentonite	0.54
28-37	0.1	Concrete	0.15
38	0.1	Grout	0.3
39-57	0.1	ILW&LLW	0.3

3.5.2 Database and program

All reactive-transport simulations were performed with PHREEQC 2.17 (Parkhurst et al. 1999) and BRGMs (Bureau de Recherches Géologiques et Minières) thermodynamic database Thermoddem (Blanc et al. 2007). Additional relevant data for mineral phases, such as molar volumes, have been selected from Lothenbach et al. (2008) and Gaucher et al. (2005) and have been validated by CEMHYD3D program (Bentz 2000), CRC handbook (Weast and Astle 1982) as well as the database MINCRYST (Chichagov 2009). See Appendix A for a more thorough summary. In order to evaluate the sensitivity of the thermodynamic database an alternative database, PCHatches (NEA 2006) was employed.

3.5.3 Model cases

The selection of modelling cases is summarized in Table 3-15. In addition to a base case (case 1) with the computational features (solid solution representation of CSH-gel, ion exchange and surface complexation, kinetics for the montmorillonite dissolution) and input data as described in Section 3.1, four alternative scenarios were analyzed in order to explore the sensitivity of the model. The sensitivity to ion transport was evaluated in case 2 and the sensitivity to dissolution model for montmorillonite in case 3. The model cases 3 and 4, attempt to evaluate the consequences of a completely fractured concrete wall, *i.e.* the innermost wall of the bentonite layer is in contact with an unlimited reservoir of cement pore water instead of solid concrete matrix. Both pore water from fresh cement and from pore water equilibrated with portlandite were employed (see Table 2-1 for composition of the pore waters).

Table 3-15. Summary of model cases. The boundary to bentonite denotes the cell adjacent to the end cells of the bentonite layer and can either be a solid matrix (shotcrete or concrete wall) representing intact concrete structures or solutions (pore water from fresh cement or pore water equilibrated with portlandite) representing completely fractured concrete structures with infinite supply of high alkaline water.

Case	1 st Boundary to bentonite	2 nd Boundary to bentonite	Diffusivity (m ² s ⁻¹)	Dissolution of montmorillonite
1	Shotcrete	Concrete wall	5.0×10^{-11}	Kinetic
2	Shotcrete	Concrete wall	5.0×10^{-10}	Kinetic
3	Shotcrete	Concrete wall	5.0×10^{-11}	Thermodynamic
4	SFR water	Pore water fresh cement	5.0×10^{-11}	Kinetic
5	SFR water	Pore water in eq. with portlandite	5.0×10^{-11}	Kinetic

4 Results

4.1 Integrity of the bentonite layer

The overall mineral composition for cross section through the Silo as predicted by the base case at year 30,000 is shown in Figure 4-1.

Although the concrete wall is partially degraded in terms of portlandite dissolution and decalcification of CSH, the montmorillonite is to a large extent unaffected. In the interfaces between shotcrete and bentonite as well as between concrete wall and bentonite, dissolved montmorillonite has been replaced by some illite, calcite, but foremost phillipsite and saponite. The encapsulated waste (ILLW/LLW) is essentially unaffected, which means that the function as buffering and determining the composition of the water that reaches the bentonite layer, is maintained throughout the period of time considered.

Confining to the bentonite layer, Figure 4-2, we note a weak pH gradient over the non-degraded part of the bentonite layer of approximately half a unit. At the interface between bentonite and concrete wall, 20 cm, of the montmorillonite has been dissolved and less than 10 cm at the interface between montmorillonite and the shotcrete. The mineral composition is similar, but much more pronounced at the interface to the concrete wall. Phillipsite dominates the mineral composition, with some fractions of gibbsite, saponite and illite. The predicted secondary phases are in agreement with those predicted in Watson et al. (2009). The evolution of the cross sections is shown in Appendix A.

Figure 4-3 show the occupancy of the interlayer exchange sites at the year 0 ($\text{Ca}_0, \text{K}_0, \text{Mg}_0, \text{Na}_0$) and at year 100,000 (Ca, K, Mg, Na). In contrast to the initial configuration, dominated by sodium, at year 100,000 the concentration of magnesium gradually decreases while sodium and calcium increase when going further into the bentonite barrier.

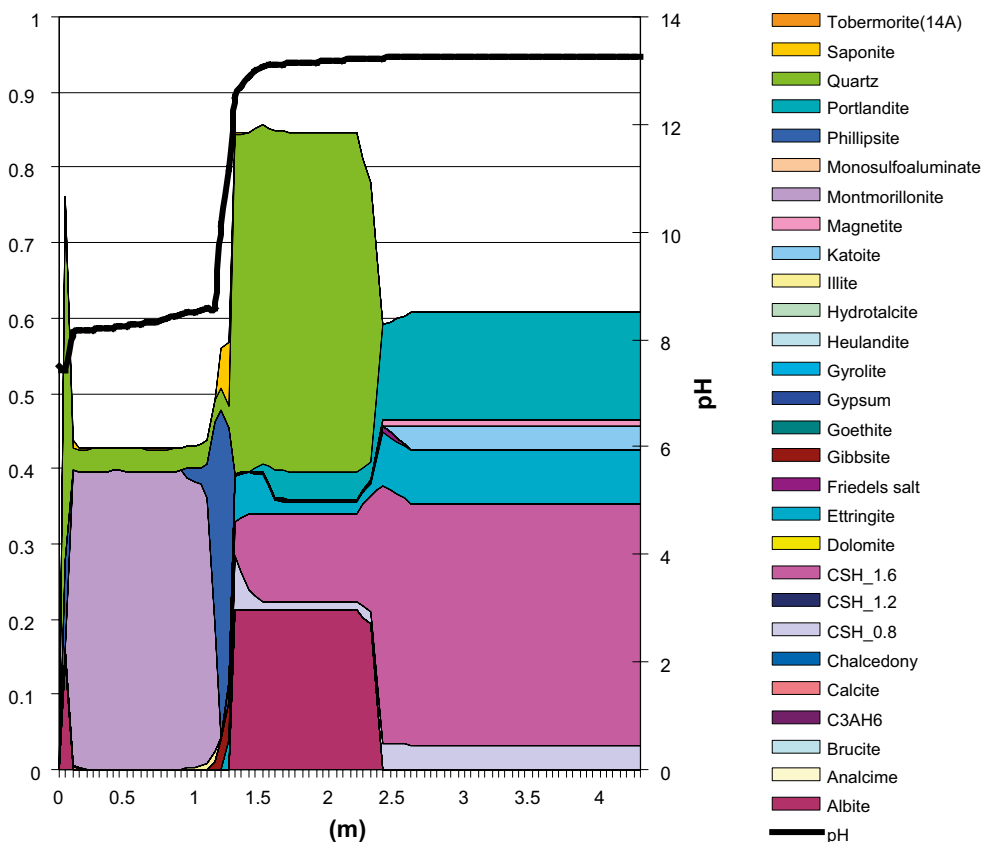


Figure 4-1. Mineral composition of a cross section of the Silo at year 30,000 as predicted by the base case.

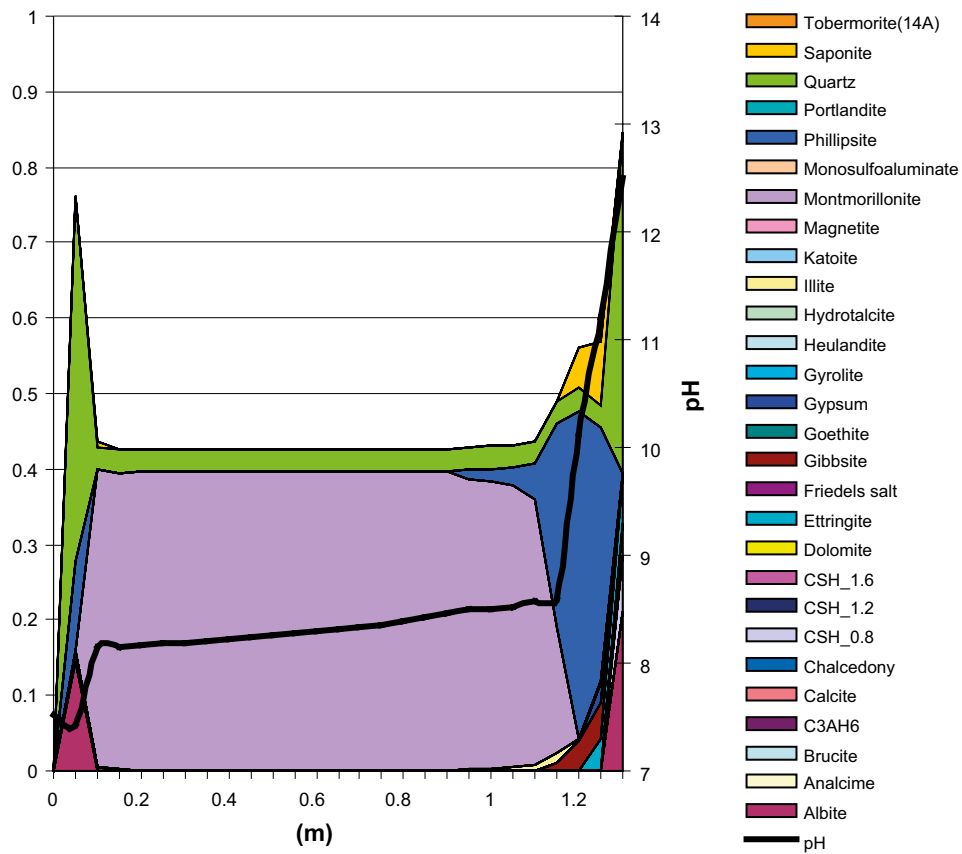


Figure 4-2. Mineral composition of a cross section of the bentonite layer of the Silo at year 30,000 as predicted by the base case.

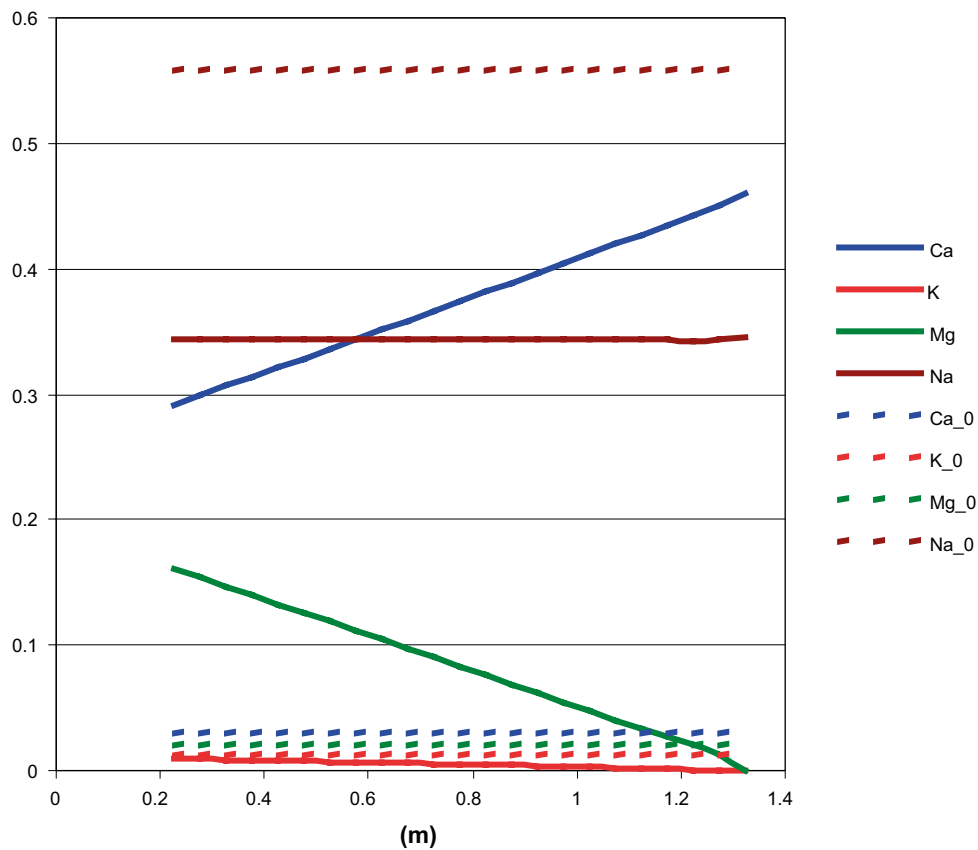


Figure 4-3. Occupancy of exchange sites at year 0 (Ca_0 , K_0 , Mg_0 , Na_0) and at year 30,000 (Ca , K , Mg , Na), (M).

With a substantially higher diffusive transport through the bentonite, the dissolution front propagates deeper into the material. As noted in 2.4.2, the estimated degradation depth for 10 times high diffusivity can be expected to be on the order of $\sqrt{10} \approx 3$ deeper than in the base case, which is in accordance with results shown in Figure 4-4. The precipitation of gibbsite, calcite and illite is more pronounced. However, a more striking feature is the conversion of montmorillonite to phillipsite is not entirely localized to the interface between bentonite and the shotcrete or the concrete wall respectively. The faster diffusion rate appears to disturb the prevailing equilibrium throughout the sample and enable a more wide spread dissolution of montmorillonite and subsequent precipitation of phillipsite. However the major part of precipitated phillipsite is found at the two interfaces.

As seen in Figure 4-5, releasing the kinetic constraint for montmorillonite dissolution, does not lead to significantly accelerated degradation. The degradation depth is similar for the model with kinetically controlled dissolution and minor differences with respect to mineral composition. In a model with purely thermodynamic montmorillonite dissolution, the precipitated phillipsite is more localized in the interface to the concrete wall and hardly any illite can be observed. In contrast to the kinetic model, there is also tobermorite starting to precipitate at the interface to concrete.

An even more rapid degradation of the bentonite barrier can be expected if the concrete is completely fractured and/or degraded from mechanisms not included in this model, thereby letting a significant higher amount of cement pore water readily available for transport into the bentonite matrix. A fractured concrete silo, which permits various flow paths through the repository, will give rise to completely different boundary conditions. Since there is no ambiguous way to estimate the extent of fractures, nor the amount pore water that will be released, the consequences of such effects are assessed through simplified scoping calculation, where the bentonite matrix is assumed to be in contact with infinite reservoirs of SFR water on one side and cement pore water on the other side. The composition of fresh cement pore water and pore water in equilibrium with portlandite are summarized in Table 2-1.

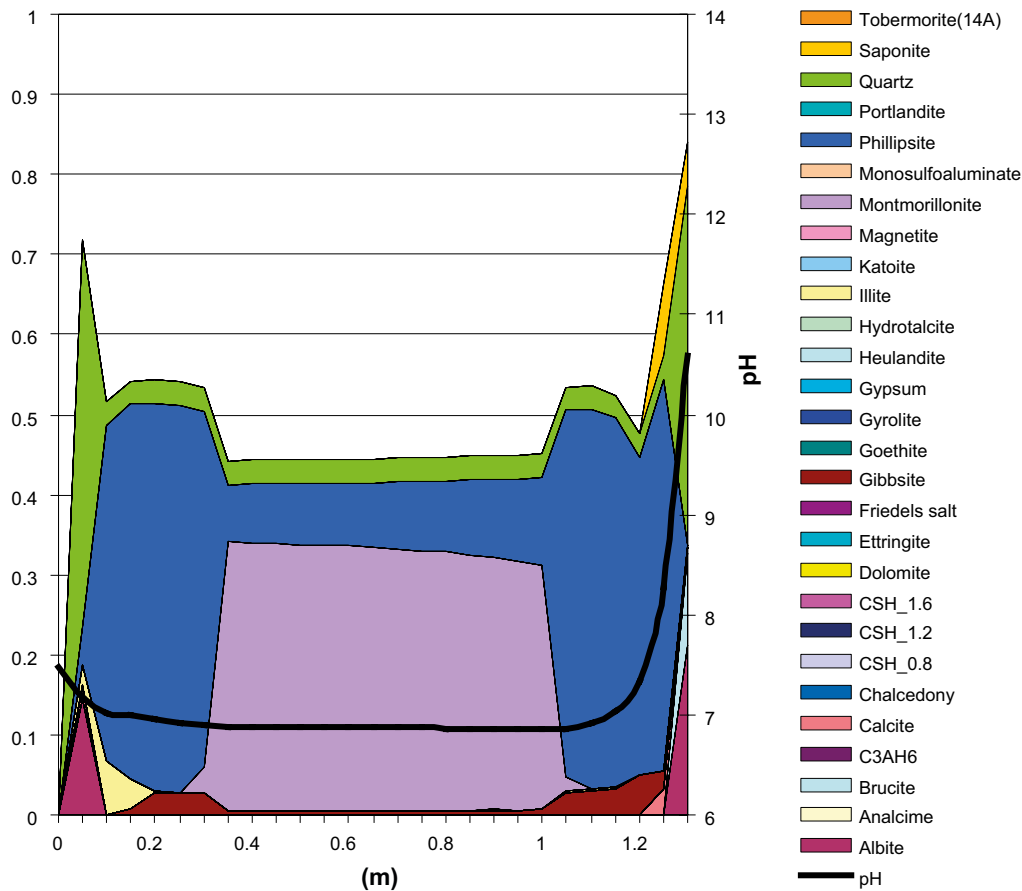


Figure 4-4. Mineral composition of a cross section of the bentonite layer of the Silo at year 30,000 for higher diffusivity, $d=5 \times 10^{-10} \text{ m}^2/\text{s}$.

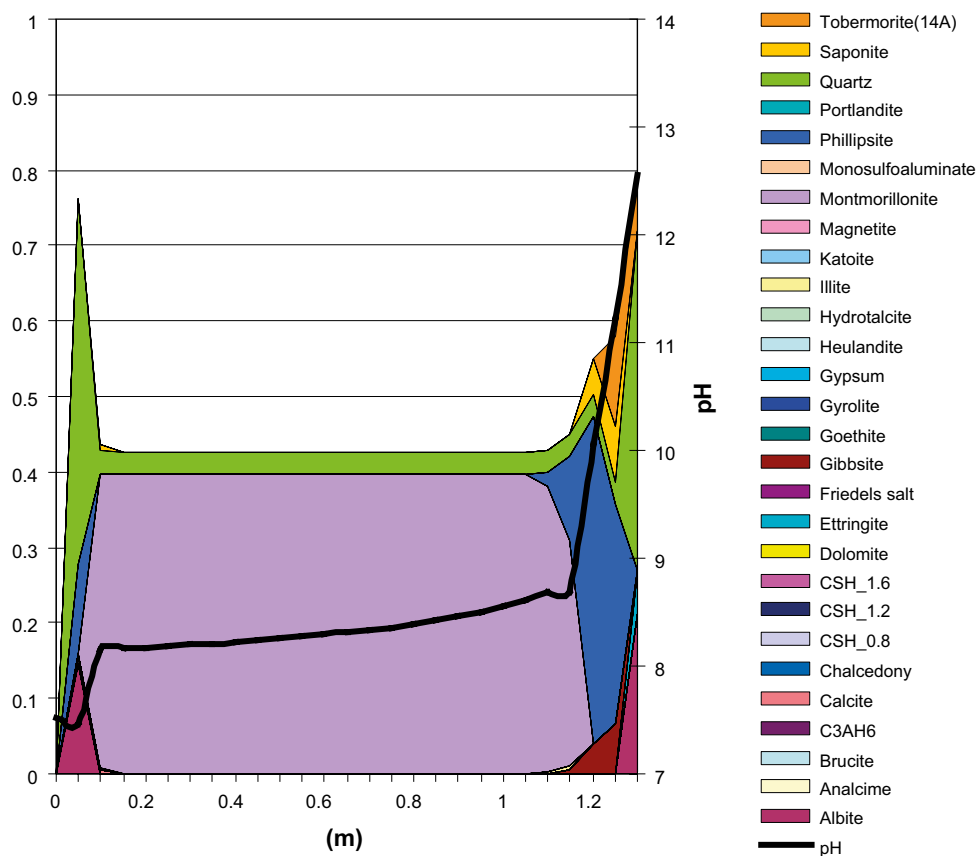


Figure 4-5. Mineral composition of a cross section of the bentonite layer of the Silo at year 30,000 for model with no kinetic constraint for montmorillonite dissolution.

Because the massive bulk of cement will retard the transport, but also regulates the composition of the water reaching the bentonite, the time scales will be magnitudes lower. Figure 4-6 to 4-7 show the cross sections at year 3,000 and 30,000 respectively for two types of cement pore water. For the most aggressive water, almost one third of the bentonite layer has been dissolved within 3,000 years and replaced by phillipsite, analcime, illite, saponite and later tobermorite.

For less aggressive water in equilibrium with portlandite the alteration effect is far less significant. The dissolution rate of montmorillonite is comparable with that obtained with an explicit concrete wall as boundary. The precipitated minerals consist of gibbsite, minor fractions of calcite, saponite and tobermorite.

For even less aggressive water in equilibrium with CSH, no alteration effect is observed within the time scale of interest. A conclusion is that the predicted dissolution and precipitation of secondary mineral phases to a large extent depends on the initial high alkaline pore water of cement, less on long-term waters stabilized with portlandite and later CSH, which is in agreement with the tolerance of bentonite to pore water exchanges shown in Figure 2-7 and Figure 2-8.

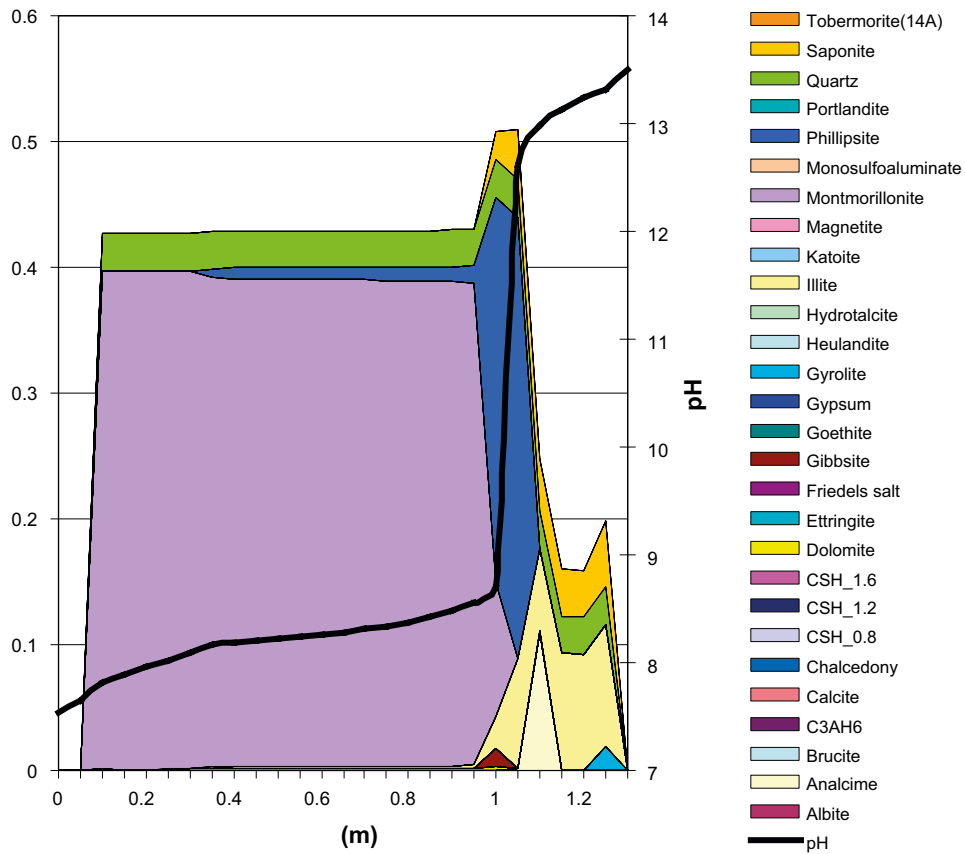


Figure 4-6. Mineral composition of a cross section of the bentonite layer of the Silo at year 3,000 when exposed to fresh cement pore water.

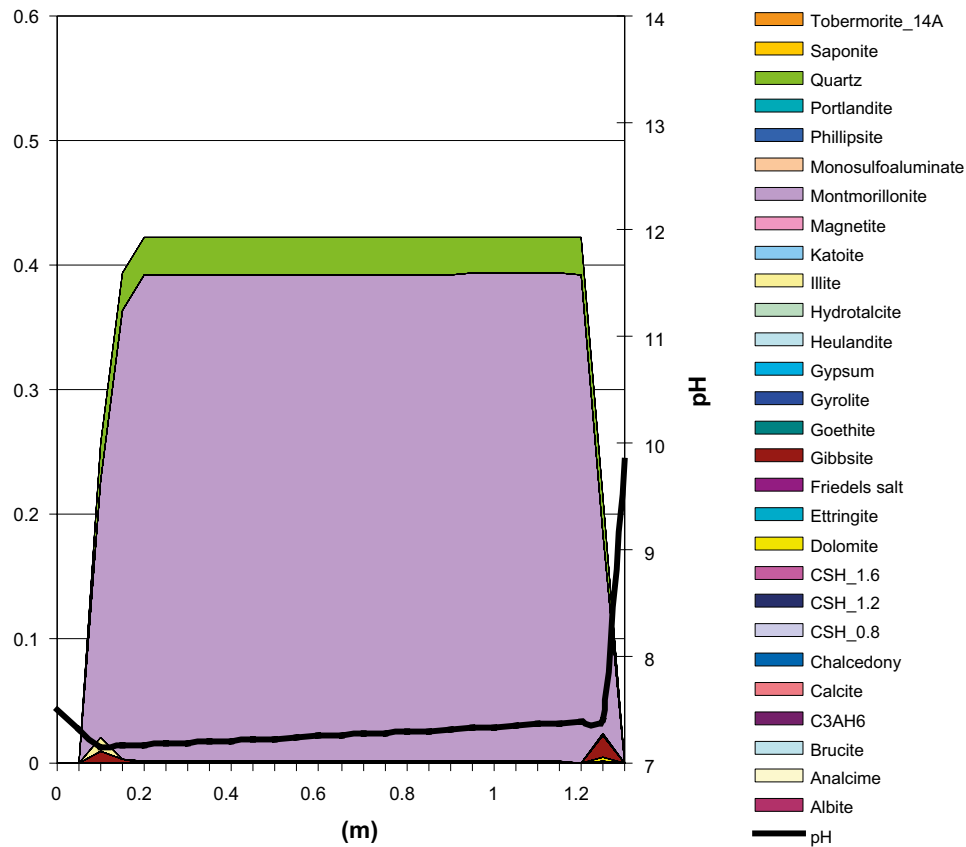


Figure 4-7. Mineral composition of a cross section of the bentonite layer of the Silo at year 30,000 when exposed to cement pore water in equilibrium with portlandite.

4.2 The composition of the water released from the repository

Since the dominating transport process within the bentonite layer is assumed to be diffusion, it is non-trivial to assess a release of water from the repository. In fact, it is not a release as much as a result of a mix between ions diffusing into the bentonite and diffusion out from the repository, and the composition will strongly depend on the volumes selected to represent the boundary conditions. The composition immediately outside the repository as predicted by model 1, is shown in Figure 4-8.

The concentration of Ca is slightly varying during the considered period of time due to dissolution of the shotcrete. However, the changes are below 10%, which probably will be negligible in comparison with the overall variation of the ambient water due to global processes, such as land uplift for instance. Overall, the changes in water composition are to a large extent determined by the dissolution of the outermost shotcrete. The bentonite layer will have a stabilizing effect on water composition outside the Silo.

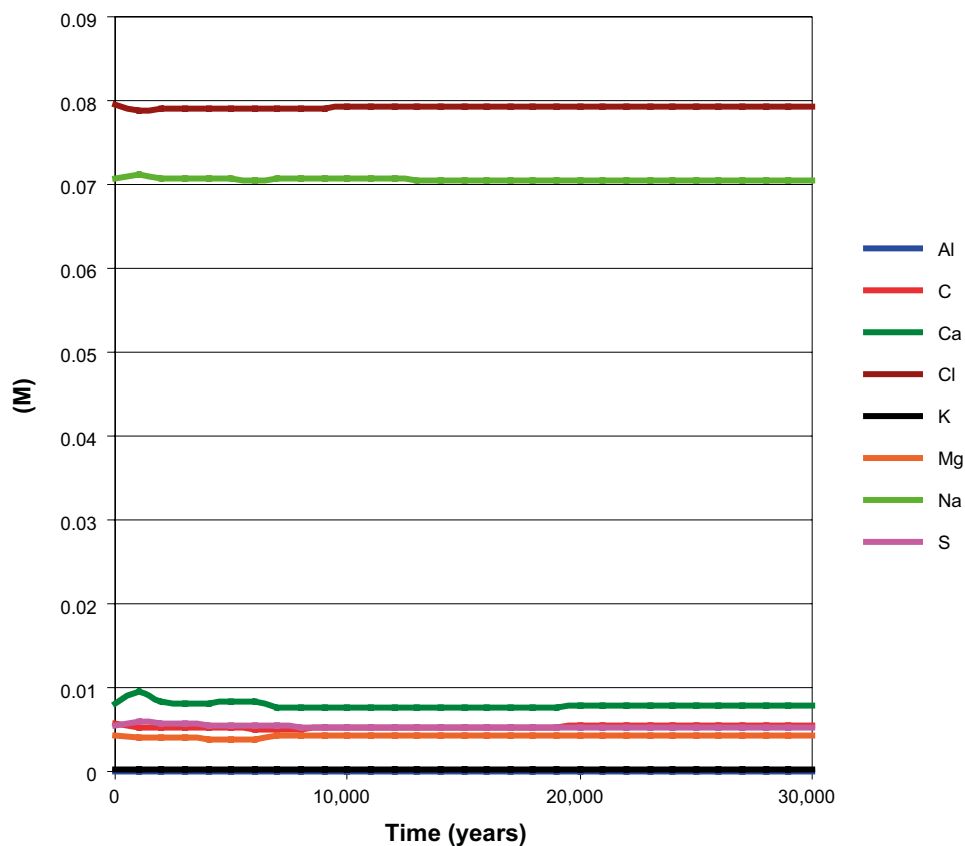


Figure 4-8. Composition of the water immediate outside the repository as a function of time as predicted by model 1 (see Table 3-8).

5 Comments and conclusions

Concrete and bentonite clay have in general been regarded as incompatible materials in repository design due to the effect of the high alkaline water released from concrete. Several modelling attempts have been made for addressing alkaline plumes in clay material, both for full scale safety assessments of repositories (Lehikoinen 2009) as well as for lab scale tests (Fernández et al. 2010, Savage et al. 2011, Watson et al. 2009). There are several unresolved difficulties when verifying model results, often related to the kinetics of secondary phases, long-term transport rate through the materials (porosity-diffusivity parameterization). A common feature is that the mineral alteration is strongly dependent on the pH and composition of the alkaline solution.

The modelling performed indicates that as long as the concrete wall is fairly intact, the degradation proceeds slowly. At year 30,000 the degradation depth is predicted to be approximately 20 cm and localized to the interface between the concrete and the bentonite. In principle the alteration depth can be assumed to scale to the mean square displacement, *i.e.* proportional to the square root of time and diffusivity. Fractured concrete on the other hand, resulting in extensive exposure to fresh cement pore water, can have a significant alteration effect on the montmorillonite. However the amount of fresh cement pore water is limited and cement pore water in equilibrium with portlandite and later CSH, has a minor effect on the dissolution rate of montmorillonite as well as the subsequent neoformation of secondary phases. From simple mass balance estimates it is noted that at least 100 volume units of concrete is needed to dissolve 1 volume unit of montmorillonite, if only the initial high alkaline water in cement pores were considered.

The employed selection of models (see Table 3-8) shows low sensitivity to kinetic model for montmorillonite dissolution, however according to scoping calculations in Section 2.4 (Figure 2-9 and Figure 2-10) there are significant differences between different thermodynamic databases, which points out directions for improvement.

The composition of the water released from the repository is rather constant throughout the period of time considered and the predicted variations are probably insignificant compared with natural variations due to more global geological processes.

5.1 Uncertainties

5.1.1 Uncertainties in mechanistic understanding

Although several rate equations have been proposed for the montmorillonite dissolution, the mechanism is not entirely understood at micro-level. Results by Takahashi et al. (2007) indicate that tetrahedral Al is dissolved before the octahedral, and concludes heterogeneous dissolution.

Reactive-transport models of repositories in general presuppose intact layers of engineered barriers, which only admit diffusive transport of ions. Various structural effects may lead to fractures and thereby increase the hydraulic conductivities and introduce flow paths through the repository. Thorough-going fractures within the engineered barrier may permit an advective flow, which will accelerate the dissolution of montmorillonite.

There may be mechanisms, presently not foreseen, that may accelerate the dissolution, because of radically different permeabilities of neoformed mineral phases.

Moreover, the kinetics, especially the kinetics of growth is not fully understood. Local-equilibrium constraints on the precipitation of secondary phases may have significant influence on the distribution of precipitated phases.

5.1.2 Model simplifications

Although the dissolution of montmorillonite is sensitive to the cation composition, the kinetic description does not explicitly include any dependence on potassium. However, as shown in comparison between different rate equations, the bulk of the material will remain in equilibrium for an extensive period of time where dissolution will be slow.

With the exception of montmorillonite, all reactions for primary and secondary minerals are governed by thermodynamic equilibrium. No kinetics constraints have been included regarding growth. Preventing a certain mineral can potentially have a dramatic effect on the mineral composition, but not on the dissolution rate (Lehikoinen 2009). Although rate parameters for numerous mineral phases have been compiled (Palandri and Kharaka 2004), there are still large uncertainties in reactive surface areas. Moreover, the composition and evolution of the ballast in the concrete is treated by a simplified kinetic reaction rate in order to achieve numerical efficiency.

Because of computational tractability and ensuring numerical stability, one single value for the diffusivity has been assumed for all species throughout the system of engineered barriers. No parameterization of porosity-diffusivity or mineral composition-diffusivity has been included, however, the moderate porosity changes imply that the application of relations of the Archie's law type, will only slightly retard the ionic transport.

Impurities in terms of soluble trace minerals and salts in the bentonite have not been considered, although pointed out (Ochs et al. 2001) as potentially important.

5.1.3 Input data and data uncertainty

As shown by the comparison between results obtained from different databases, the thermodynamic description has a substantial influence on the predicted degradation sequence. The inconsistencies between databases call for a critical test of available thermodynamic databases against validated experimental data.

Although transport related parameters such as cation exchange and surface complexation are of great importance for estimation of radionuclide release, their influence on the degradation rate of bentonite is not significant. In comparison with other parameters, they are also well characterized. Diffusivities for the barrier will depend on the initial state, but also the evolution of the mineral composition, however, as shown by comparison between models with different diffusivities and by Gaucher and Blanc (2006) and Gaucher et al. (2005), increasing diffusion rate does not alter the mineral composition, but the dissolution rate, typically in proportion to the square root of time.

The composition of the infiltrating water has an influence on the composition of the degraded barrier, but not considerably on the degradation rate, as shown by comparison between Figure 4-4 and 4-7. The initial conditions in terms of the composition of barriers may differ within 10–20% without any significant changes in the modelling results obtained.

5.1.4 Overall uncertainties

The major uncertainties can be traced to the selected thermodynamic database, the growth kinetics, unknown factors that may reduce the swelling pressure and thereby allowing local flows through the bentonite barrier.

In order to improve predictions it would be necessary to include growth kinetics and assess the influence through rigorous sensitivity analysis. Moreover, the differences between results obtained from Thermoddem and PCHatches database call for a critical test of a wide selection of databases against experimental data where no transport parameters can interfere with the comparisons.

References

SKB's (Svensk Kärnbränslehantering AB) publications can be found at www.skb.se/publications.

- Andersson K E, Allard B, Bengtsson M, Magnusson B, 1989.** Chemical composition of cement pore solutions. *Cement and Concrete Research* 19, 327–332.
- Appelo C A J, Van Loon L R, Wersin P, 2010.** Multicomponent diffusion of a suite of tracers (HTO, Cl, Br, I, Na, Sr, Cs) in a single sample of Opalinus Clay. *Geochimica et Cosmochimica Acta* 74, 1201–1219.
- Arcos D, Bruno J, Karnland O, 2003.** Geochemical model of the granite–bentonite–groundwater interaction at Äspö HRL (LOT experiment). *Applied Clay Science* 219–228.
- Bentz D P, 2000.** CEMHYD3D: A three-dimensional cement hydration and microstructure development modelling package. Version 2.0. National Institute of Standards and Technology Interagency Report 7232, U.S. Department of Commerce.
- Berner U, 1992.** Evolution of pore water chemistry during degradation of cement in a radioactive waste repository environment. *Waste Management* 12, 201–219.
- Birgersson M, Karnland O, 2009.** Ion equilibrium between montmorillonite interlayer space and an external solution – Consequences for diffusional transport. *Geochimica et Cosmochimica Acta* 73, 1908–1923.
- Blanc P, Lassin A, Piantone P, 2007.** Thermoddem a database devoted to waste minerals. Orléans, France: BRGM. Available at: <http://thermoddem.brgm.fr>
- Bourg I C, Bourg A C, Sposito G, 2003.** Modeling diffusion and adsorption in compacted bentonite: a critical review. *Journal of Contaminant Hydrology* 61, 293–302.
- Bourg I C, Sposito G, Bourg A C M, 2007.** Modeling the acid–base surface chemistry of montmorillonite. *Journal of Colloid and Interface Science* 312, 297–310.
- Bradbury M H, Baeyens B, 1997.** A mechanistic description of Ni and Zn sorption on Na-montmorillonite. Part II: modelling. *Journal of Contaminant Hydrology* 27, 223–248.
- Bradbury M H, Baeyens B, 2002.** Porewater chemistry in compacted re-saturated MX-80 bentonite: physico-chemical characterisation and geochemical modelling. Nagra Technical Report NTB-01-08, Nagra, Switzerland.
- Bradbury M H, Baeyens B, 2003.** Porewater chemistry in compacted re-saturated MX-80 bentonite. *Journal of Contaminant Hydrology* 61, 329–338.
- Bradbury M H, Baeyens B, 2009.** Experimental and modelling studies on the pH buffering of MX-80 bentonite porewater. *Applied Geochemistry* 24, 419–425.
- Cama J, Ganor J, Ayora C, Lasaga C A, 2000.** Smectite dissolution kinetics at 80°C and pH 8.8. *Geochimica et Cosmochimica Acta* 64, 2701–2717.
- Chávez-Páez M, Van Workum K, de Pablo L, de Pablo J J, 2001.** Monte Carlo simulations of Wyoming sodium montmorillonite hydrates. *Journal of Chemical Physics* 114, 1405.
- Chichagov A V, 2009.** WWW – MINCRYST. Crystallographic and crystallochemical database for mineral and their structural analogues Chernogolovka, Russia: IEM RAS. Available at: <http://database.iem.ac.ru/mincryst/>
- Cronstrand P, 2007.** Modelling the long-time stability of the engineered barriers of SFR with respect to climate changes. SKB R-07-51, Svensk Kärnbränslehantering AB.
- Elliott W C, Matisoff G, 1996.** Evaluation of kinetic models for the smectite to illite transformation. *Clays and Clay Minerals* 44, 77–87.
- Fernández R, Cuevas J, Mäder U K, 2010.** Modeling experimental results of diffusion of alkaline solutions through a compacted bentonite barrier. *Cement and Concrete Research* 40, 1255–1264.





























- Fujiwara A, Takegahara T, Chiba T, Ikeda T, Takase H, Savage D, Metcalfe R, 2003.** Kinetic controls on cement porefluid–bentonite interactions in engineered barrier: new insights from experimental and numerical simulations. *Clays In natural and engineered barriers for radioactive waste confinement*. International Meeting, Reims, France, 9–12 December 2002. Available at: http://www.iaea.org/inis/collection/NCLCollectionStore/_Public/35/015/35015648.pdf
- Gaucher E C, Blanc P, 2006.** Cement/clay interactions – A review: experiments, natural analogues and modelling. *Waste Management* 26, 776–788.
- Gaucher E, Tournassat C, Nowak C, 2005.** Modelling the geochemical evolution of the multi-barrier system of the Silo of the SFR repository. Final report. SKB R-05-80, Svensk Kärnbränslehantering AB.
- Hedström M, Karnland, 2012.** Donnan equilibrium in Na-montmorillonite from a molecular dynamics perspective. *Geochimica et Cosmochimica Acta* 77, 266–274.
- Huang W-L, 1992.** Illitic clay formation during experimental diagenesis of arkoses. In Houseknecht D W, Pittman E D (eds). *Origin, diagenesis and petrophysics of clay minerals in sandstones*. Tulsa: Society for Sedimentary Geology. (SEPM Special Publication 47), 49–63.
- Huertas F J, Caballero E, Jiménez de Cisneros C, Huertas F, Linares J, 2001.** Kinetics of montmorillonite dissolution in granitic solutions. *Applied Geochemistry* 16, 397–407.
- Karnland O, 2010.** Chemical and mineralogical characterization of the bentonite buffer for the acceptance control procedure in a KBS-3 repository. SKB TR-10-60, Svensk Kärnbränslehantering AB.
- Karnland O, Birgersson M, 2006.** Montmorillonite stability. With special respect to KBS-3 conditions. SKB TR-06-11, Svensk Kärnbränslehantering AB.
- Karnland O, Olsson S, Nilsson U, 2006.** Mineralogy and sealing properties of various bentonites and smectite-rich clay materials. SKB TR-06-30, Svensk Kärnbränslehantering AB.
- Kozaki T, Inada Koichi, Sato S, Ohashi H, 2001.** Diffusion mechanism of chloride ions in sodium montmorillonite. *Journal of Contaminant Hydrology* 47, 159–170.
- Kozaki T, Fujishima A, Saito N, Sato S, Ohashi H, 2005.** Effects of dry density and exchangeable cations on the diffusion process of sodium ions in compacted montmorillonite. *Engineering Geology* 81, 246–254.
- Lehikoinen J, 2009.** Bentonite–cement interaction – preliminary results from model calculations. Posiva Working Report 2009-37, Posiva Oy, Finland.
- Leroy P, Revil A, Coelho D, 2006.** Diffusion of ionic species in bentonite. *Journal of Colloid and Interface Science* 296, 248–255.
- Lothenbach B, Matschei T, Möschner G, Glasser F, 2008.** Thermodynamic modelling of the effect of temperature on the hydration and porosity of Portland cement. *Cement and Concrete Research* 38, 1–18.
- Marty N C M, Cama J, Sato T, Chino D, Villieras F, Razafitianamaharavo A, Brendlé J, Giffaut E, Soler J M, Gaucher E C, Tournassat C, 2011.** Dissolution kinetics of synthetic Na-smectite. An integrated experimental approach. *Geochimica et Cosmochimica Acta* 75, 5849–5864.
- Melkior T, Mourzagh D, Yahiaoui S, Thoby D, Alberto J C, Brouard C, Michau N, 2004.** Diffusion of an alkaline fluid through clayey barriers and its effect on the diffusion properties of some chemical species. *Applied Clay Science* 26, 99–107.
- Muurinen A, 2009.** Studies on the chemical conditions and microstructure in the reference bentonites of alternative buffer materials project (ABM) in Äspö. Posiva Working Report 2009-42, Posiva Oy, Finland.
- Nakayama S, Sakamoto Y, Yamaguchi T, Akai M, Tanaka T, Sato T, Iida Y, 2004.** Dissolution of montmorillonite in compacted bentonite by highly alkaline aqueous solutions and diffusivity of hydroxide ions. *Applied Clay Science* 27, 53–65.
- NEA, 2006.** ZZ-HATCHES-17. NEA-1210/18, OECD/NEA.

- Ochs M, Lothenbach B, Wanner H, Sato H, Yui M, 2001.** An integrated sorption–diffusion model for the calculation of consistent distribution and diffusion coefficients in compacted bentonite. *Journal of Contaminant Hydrology* 47, 283–296.
- Ochs M, Talerico C, Sellin P, Hedin A, 2006.** Derivation of consistent sorption and diffusion parameters and their uncertainties for compacted MX-80 bentonite. *Physics and Chemistry of the Earth* 31, 600–609.
- Palandri J L, Kharaka Y K, 2004.** A compilation of rate parameters of water– mineral interaction kinetics for application to geochemical modelling. Open File Report 2004-1068, United States Geological Survey, Menlo Park, California.
- Parkhurst D L, Appelo C A J, 1999.** User’s guide to PHREEQC (version 2): a computer program for speciation, batch-reaction, one-dimensional transport, and inverse geochemical calculations. Water-Resources Investigations Report 99-4259, U.S. Geological Survey, Denver, Colorado.
- Pusch R, 1993.** Evolution of models for conversion of smectite to non-expandable minerals. SKB TR 93-33, Svensk Kärnbränslehantering AB.
- Pusch R, Erlström M, Börgesson L, 1985.** Sealing of rock fractures. A survey of potential useful methods and substances. SKB TR 85-17, Svensk Kärnbränslehantering AB.
- Pusch R, Kasbohm J, Thao H T M, 2009.** Chemical stability of montmorillonite buffer clay under repository-like conditions – A synthesis of relevant experimental data. *Applied Clay Science* 47, 113–119.
- Pytte A M, Reynolds R C, 1989.** The thermal transformation of smectite to illite. In Naeser, N D, McCulloh T H (eds). *Thermal history of sedimentary basins*. New York: Springer-Verlag, 133–140.
- Rimstidt J D, Barnes H L, 1980.** The kinetics of silica–water reactions. *Geochimica et Cosmochimica Acta* 44, 1683–1699.
- Rozalén M L, Huertas F J, Brady P V, Cama J, García-Palma S, Linares J, 2008.** Experimental study of the effect of pH on the kinetics of montmorillonite dissolution at 25°C. *Geochimica et Cosmochimica Acta* 72, 4224–4253.
- Rozalén L, Brady P V, Huertas F J, 2009.** Surface chemistry of K-montmorillonite: ionic strength, temperature dependence and dissolution kinetics. *Journal of Colloid and Interface Science* 333, 474–484.
- Sato T, Kuroda M, Yokoyama S, Fukushi K, Tanaka T, Nakayama S, 2003.** Mechanism and kinetics of smectite dissolution under alkaline conditions. *Geochimica et Cosmochimica Acta* 67, A415.
- Sato H, 2008.** Thermodynamic model on swelling of bentonite buffer and backfill materials. *Physics and Chemistry of the Earth, Parts A/B/C* 33, S538–S543.
- Savage D, Noy D, Mihara M, 2002.** Modelling the interaction of bentonite with hyperalkaline fluids. *Applied Geochemistry* 17, 207–223.
- Savage D, Walker C, Arthur R, Rochelle C, Oda C, Takase H, 2007.** Alteration of bentonite by hyperalkaline fluids: a review of the role of secondary minerals. *Physics and Chemistry of the Earth* 32, 287–297.
- Savage D, Arthur R, Watson C, Wilson J, Strömberg B, 2011.** Testing geochemical models of bentonite pore water evolution against laboratory experimental data. *Physics and Chemistry of the Earth* 36, 1817–1829.
- SKB, 2008.** Safety analysis SFR 1. Long-term safety. SKB R-08-130, Svensk Kärnbränslehantering AB.
- Skipper N T, Chou Chang F-R, Sposito G, 1995.** Monte Carlo simulations of interlayer molecular structure in swelling clay minerals. 1. Methodology. *Clays and Clay Minerals* 43, 285–293.
- Takahashi T, Ohkubo T, Suzuki K, Ikeda Y, 2007.** High resolution solid-state NMR studies on dissolution and alteration of Na-montmorillonite under highly alkaline conditions. *Microporous and Mesoporous Materials* 106, 284–297.
- Tournassat C, Appelo C A J, 2011.** Modelling approaches for anion-exclusion in compacted. Na-bentonite. *Geochimica et Cosmochimica Acta* 75, 3698–3710.

- Van Loon L R, Glaus M A, Muller W, 2007.** Anion exclusion effects in compacted bentonites: towards a better understanding of anion diffusion. *Applied Geochemistry* 22, 2536–2552.
- Velde B, Vasseur G, 1992.** Estimation of the diagenetic smectite to illite transformation in time-temperature space. *American Mineralogist* 77, 967–976.
- Watson C, Hane K, Savage D, Benbow S, Cuevas J, Fernandez R, 2009.** Reaction and diffusion of cementitious water in bentonite: results of ‘blind’ modelling. *Applied Clay Science* 45, 54–69.
- Weast R C, Astle M J (eds), 1982.** CRC handbook of chemistry and physics. 63rd ed. Cleveland, OH: CRC Press.
- Wersin P, Curti E, Appelo C A J, 2004.** Modelling bentonite–water interactions at high solid/liquid ratios: swelling and diffuse double layer effects. *Applied Clay Science* 26, 249– 257.
- Yamaguchi T, Sakamoto Y, Akai M, Takazawa M, Iida Y, Tanaka T, Nakayama S, 2007.** Experimental and modeling study on long-term alteration of compacted bentonite with alkaline groundwater. *Physics and Chemistry of the Earth* 32, 298–310.
- Yamaguchi T, Yamada F, Negishi K, Hoshino S, Mukai M, Tanaka T, Nakayama S, 2008.** Development and verification of a reactive transport model for long-term alteration of bentonite–cement–seawater systems. *Physics and Chemistry of the Earth* 33, Supplement 1, S285–S294.

Summary of input data for primary and secondary mineral phases

Table A-1. A selection of primary and secondary minerals phases, their log k value within the Thermoddem database, molar volume and colour code employed in figures in Appendix B.

Mineral	Formula	log k	Molar volume (cm ³ mol ⁻¹)	Colour code
Albite	NaAlSi ₃ O ₈	2.74	100.25	
Analcime	Na _{0.99} Al _{0.99} Si _{2.01} O ₆ ·H ₂ O	16.64	98.281	
Brucite	Mg(OH) ₂	16.85	24.63	
C3AH6	Ca ₃ Al ₂ O ₆ ·6H ₂ O	80.8	150.0	
Calcite	CaCO ₃	-8.47	36.93	
Chalcedony	SiO ₂	-3.45	60.084	
CSH _{1.6}	C _{1.8} S _{3.8} H	32.4	108.0	
CSH _{1.2}	C _{1.1} S _{3.1} H	16.66	101.8	
CSH _{0.8}	C _{0.8} S _{2.8} H	11.03	101.8	
Dolomite	CaMg(CO ₃) ₂	3.53	64.929	
Ettringite	Ca ₆ Al ₂ (SO ₄) ₃ (OH) ₁₂ ·26H ₂ O	57.0	709.09	
Friedelsalt	Ca ₄ A ₂ Cl ₂ O ₁₆ H ₂ O	70.72	296.66	
Gibbsite	Al(OH) ₃	7.73	33.33	
Goethite	FeOOH	-8.13	23.38	
Gypsum	CaSO ₄ ·2H ₂ O	-4.61	73.89	
Gyrolite	Ca ₂ Si ₃ O _{7.5} (OH) ₂ ·2H ₂ O	22.34	136.06	
Heulandite	Ca _{1.07} Al _{2.14} Si _{6.86} O ₁₈ ·6.17H ₂ O	2.460	313.97	
Hydrotalcite	Mg ₄ Al ₂ O ₁₇ ·H ₂ O	75.34	215.21	
Illite	K _{0.6} Mg _{0.25} Al _{1.8} Al _{0.5} Si _{3.5} O ₁₁ ·H ₂ O	10.44	144.87	
Katoite	Ca ₃ Al ₂ SiO ₁₂ H ₈	6.471	150.13	
Magnetite	Fe ₃ O ₄	-6.62	44.96	
Montmorillonite	Na _{0.33} Mg _{0.33} Al _{1.67} Si ₄ O ₁₀ (OH) ₂	1.32	155.84	
Monosulfoaluminate	Ca ₄ Al ₂ (SO ₄)O ₁₈ H ₂₄	70.25	313.0	
Phillipsite	NaAlSi ₃ O ₈ ·3H ₂ O	1.360	143.76	
Portlandite	Ca(OH) ₂	22.81	33.1	
Quartz	SiO ₂	-3.74	22.93	
Saponite-Na	Na _{0.33} Mg ₃ Al _{0.33} Si _{3.67} O ₁₀ (OH) ₂	27.09	136.69	
Tobermorite(14A)	Ca ₅ Si ₆ H ₂₁ O ₂₇	62.94	356.61	

Evolution of the bentonite barrier

Appendix B contains the results of the reactive transport modelling visualized in terms of cross sections describing mineralogy and pH for the bentonite layer in the Silo at year 1,000, 5,000, 10,000, 15,000, 20,000, 25,000 and 30,000. The cell most to the left represents the shotcrete and the cell most to the right the boundary to the concrete wall.

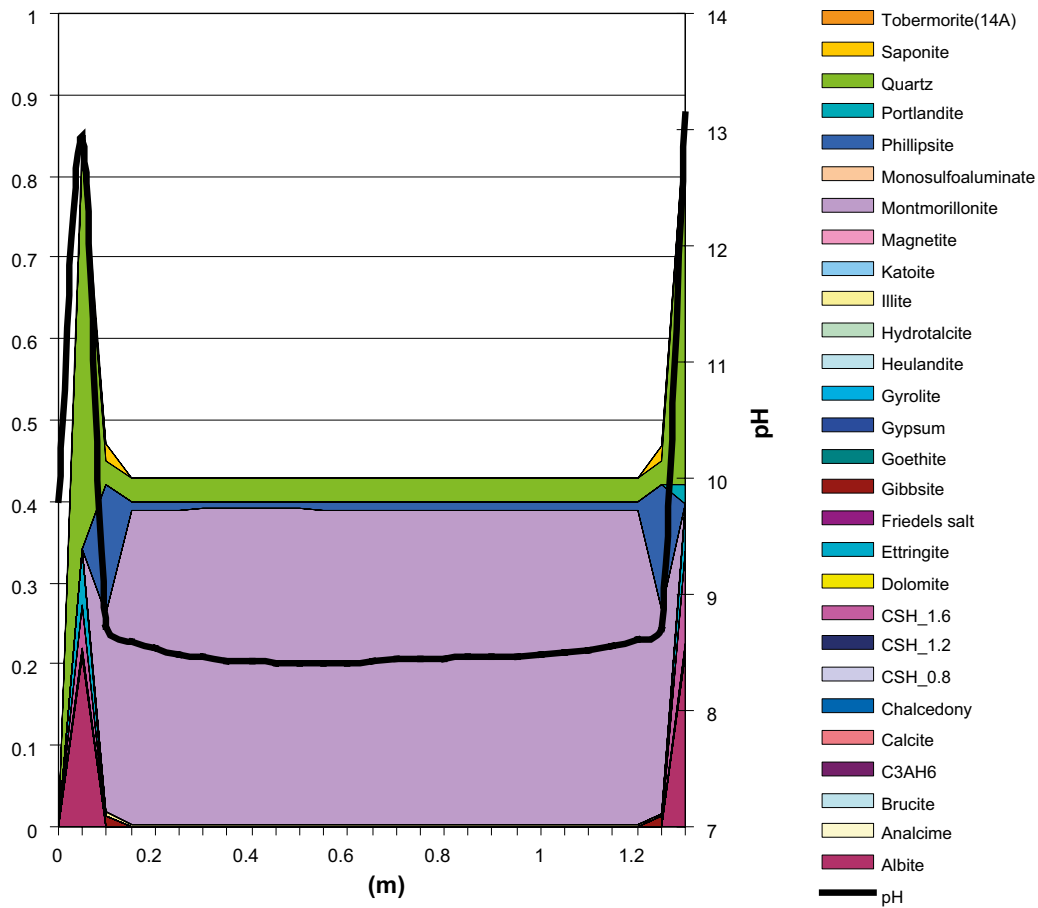


Figure B-1. Mineralogy and pH for the bentonite layer in the Silo at year 1,000.

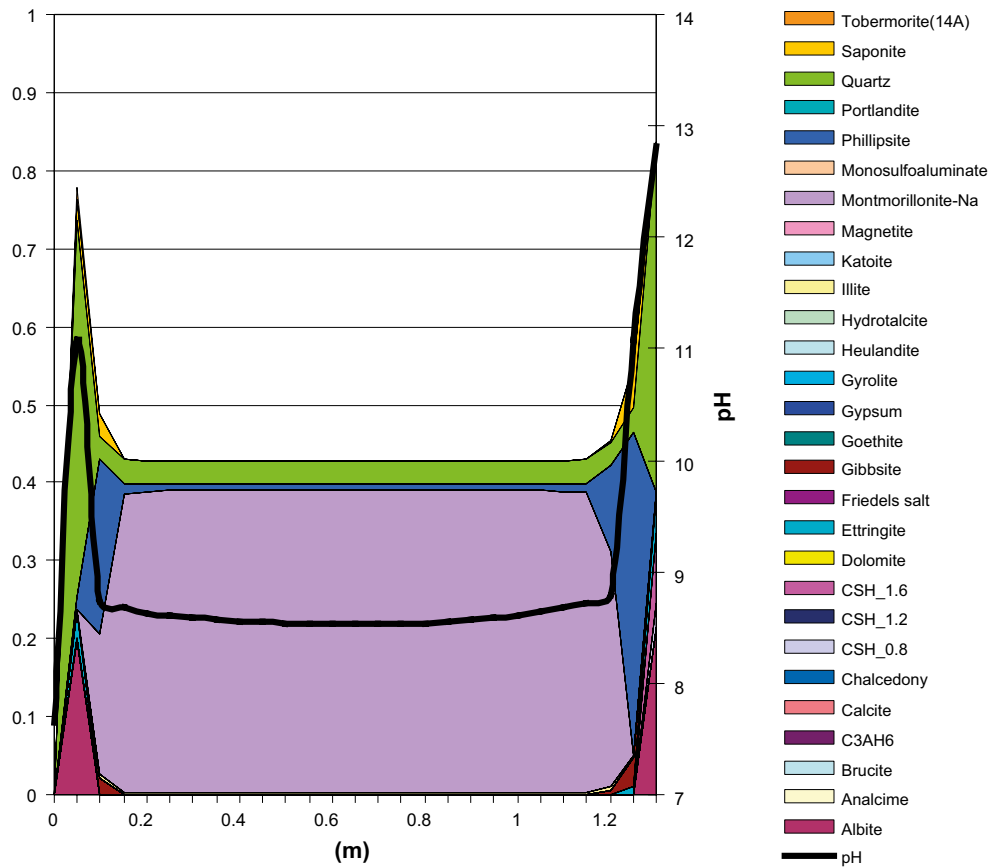


Figure B-2. Mineralogy and pH for the bentonite layer in the Silo at year 5,000.

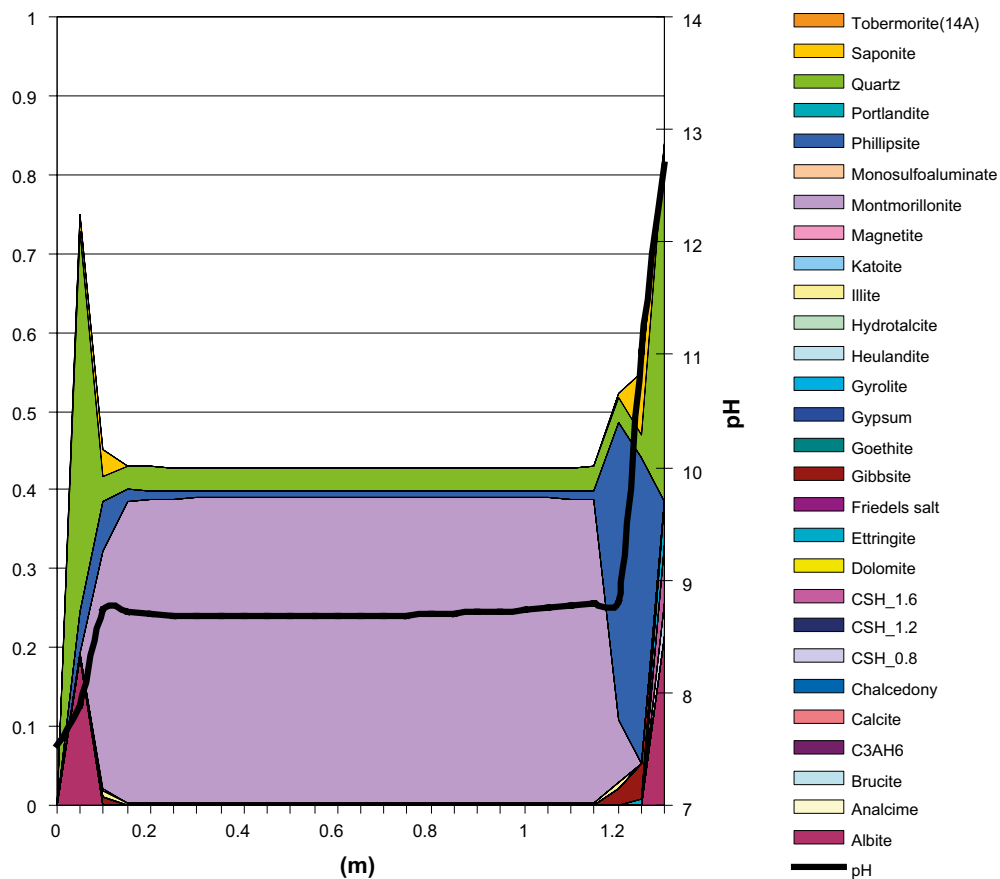


Figure B-3. Mineralogy and pH for the bentonite layer in the Silo at year 10,000.

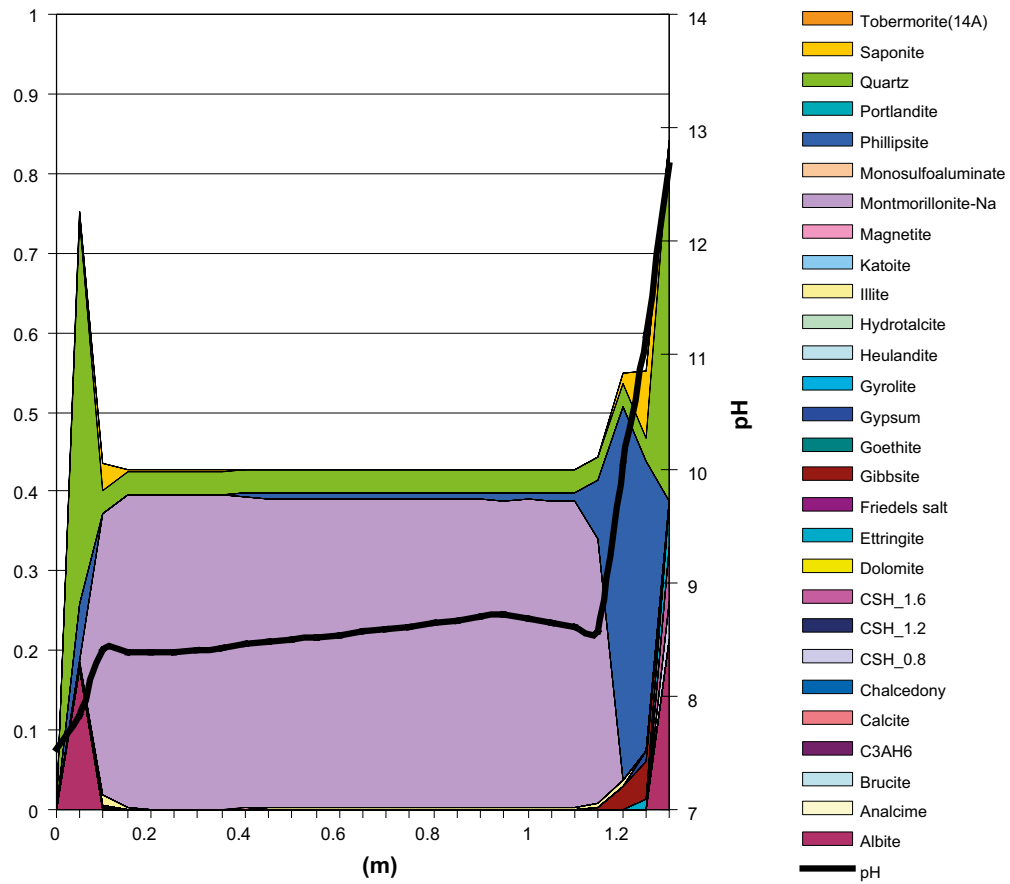


Figure B-4. Mineralogy and pH for the bentonite layer in the Silo at year 15,000.

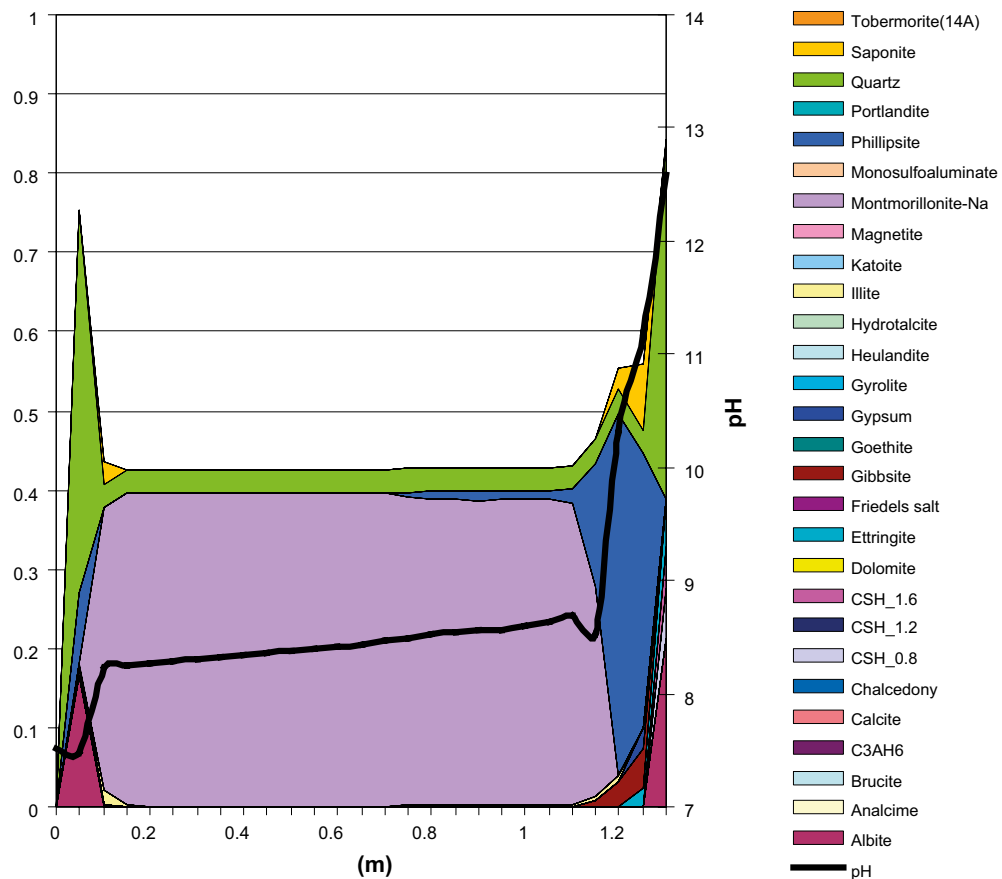


Figure B-5. Mineralogy and pH for the bentonite layer in the Silo at year 20,000.

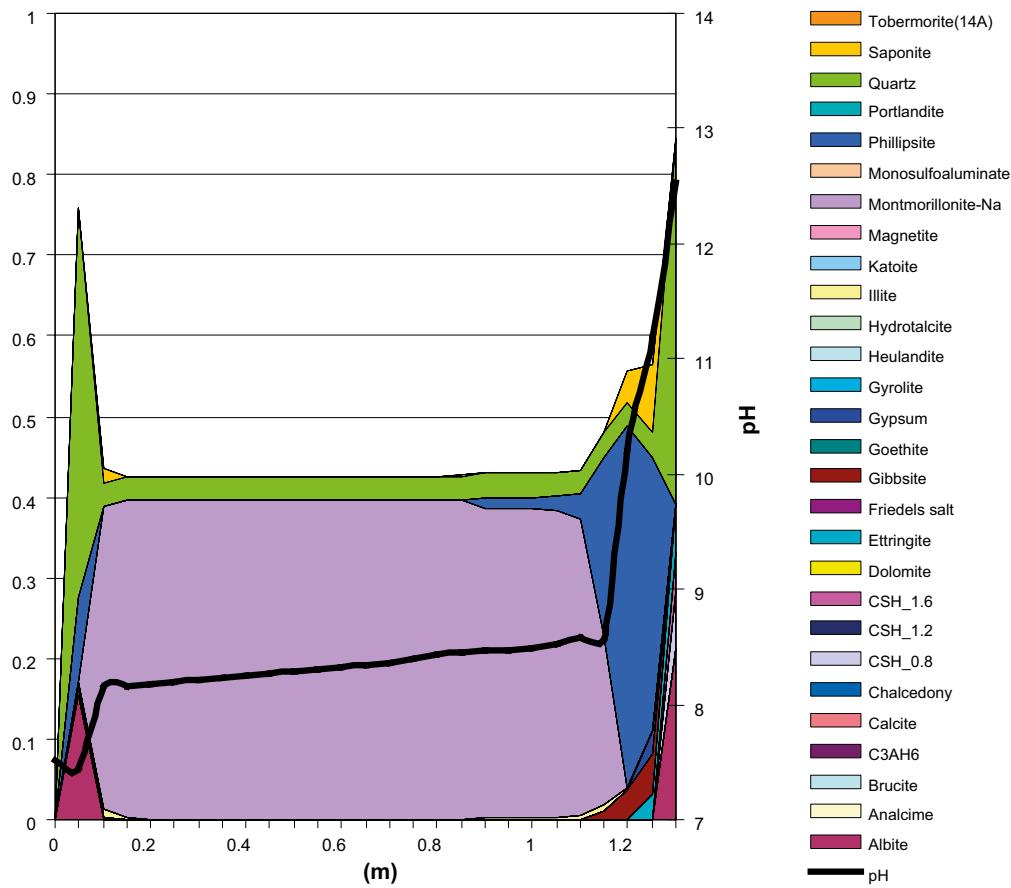


Figure B-6. Mineralogy and pH for the bentonite layer in the Silo at year 25,000.

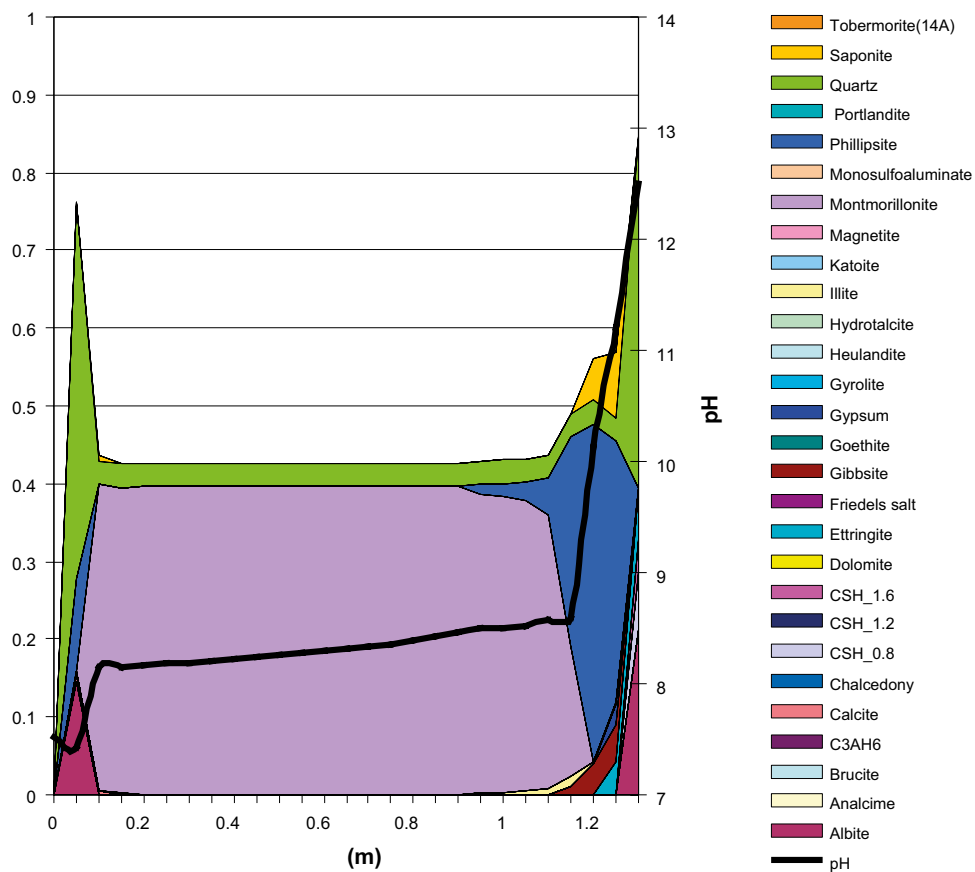


Figure B-7. Mineralogy and pH for the bentonite layer in the Silo at year 30,000.